RESEARCH ARTICLE
SOLID EARTH: SEISMOLOGY

Earth and Planetary Physics
10: 223–238, 2026
doi: 10.26464/epp2026019

Regional-scale full 3D hybrid waveform forward modeling

JingNan Sun[1], Yi Wang[2*], Li Zhao[1,3], and RiSheng Chu[2]

[1]School of Earth and Space Sciences, Peking University, Beijing 100871, China;

[2]State Key Laboratory of Precision Geodesy, Innovation Academy for Precision Measurement Science and Technology, Chinese Academy of Sciences, Wuhan 430077, China;

[3]Hebei Hongshan National Geophysical Observatory for Thick Sediments and Seismic Hazards, Peking University, Beijing 100871, China

Key Points:

- A regional-scale full three-dimensional hybrid waveform modeling method is developed to efficiently update the source-region velocity.
- Fitting of high-frequency waveform records reveals a pronounced shallow sedimentary layer in the Changning area.
- Finite-fault modeling from InSAR inversion better captures rupture directivity and improves the near-field waveform fits compared with a point source.

Citation: Sun, J. N., Wang, Y., Zhao, L., and Chu, R. S. (2026). Regional-scale full 3D hybrid waveform forward modeling. *Earth Planet. Phys.*, *10*(2), 223–238. http://doi.org/10.26464/epp2026019

Abstract: Accurate three-dimensional (3D) velocity models are essential for fitting high-frequency seismic waveform records. This process usually requires regional-scale 3D numerical simulations that are computationally expensive, especially with sparse seismic networks. Because of the significance of source domain modeling, we propose a hybrid waveform simulation approach that combines the 3D spectral-element method (SEM) with the displacement representation theorem. By separating near-source wavefield excitation from long-distance wave propagation to stations, only the source domain wavefield needs to be recomputed when the local velocity and source models change. We apply the method to the 2019 M_w 5.0 Changning shallow earthquake to verify its flexibility and effectiveness. We compare high-frequency waveforms computed with different regional velocity models against observations. Results show that the hybrid method achieves accuracy comparable to full SEM 3D simulations while reducing computation costs by more than two orders of magnitude when the structure of the source region updates. Our results further indicate that high-frequency waveforms are highly sensitive to shallow structures. Introducing low-velocity shallow layers into the source region improves near-field waveform fits, indicating pronounced low-velocity sediments in the Changning area. Large surface-wave time delays suggest that shallow velocities within the Sichuan Basin are lower than those in existing published models. In addition, an Interferometric Synthetic Aperture Radar (InSAR)-derived finite-fault model outperforms the point-source model in near-field waveform fitting and better reproduces rupture directivity. The proposed method is practical for high-frequency waveform modeling in areas with complex subsurface structures and rupture processes.

Keywords: wave modeling; hybrid simulation; strain Green's tensor

1. Introduction

Accurate determination of source parameters is crucial for understanding rupture mechanisms and dynamics (Shi QB et al., 2018). Source parameters can be determined by waveform-based inversion methods, such as the cut-and-paste (CAP) method (Zhu LP and Helmberger, 1996; Zhu LP and Ben-Zion, 2013; Chu RS and Sheng MH, 2023), which have been widely applied in studies of moderate and strong earthquakes (Zhao LS and Helmberger, 1994). The reliability of waveform fitting relies on accurate three-dimensional (3D) velocity models and full 3D simulation methods (Fichtner and Tkalčić, 2010; Gallovič et al., 2010), especially in the high-frequency range (Qian YY et al., 2019a, b; Zhang L et al., 2022). However, seismic networks are usually sparse, and many earthquakes tend to occur in limited areas. This situation is common in both teleseismic and regional earthquake studies, where full-domain 3D waveform simulations are expensive, with costs that scale roughly with the fourth power of regional size and target frequency.

To address this problem, various hybrid simulation strategies have been proposed and applied to teleseismic source studies (Wu WB et al., 2018; Lyu C et al., 2022, 2025; Qian YY et al., 2024; Zang C et al., 2024; Liu TS et al., 2025). These methods typically use high-accuracy numerical simulations in the source region (e.g., 3D spectral-element modeling) while adopting approximate forward techniques (e.g., a one-dimensional [1D] background model or ray-

First author: J. N. Sun, jingnan233@pku.edu.cn
Correspondence to: Y. Wang, wangyi@apm.ac.cn
Received 12 SEP 2025; Accepted 20 NOV 2025.
First Published online 30 DEC 2025.

based travel-time methods) for long-distance wave propagation, with wavefields coupled at a virtual boundary. This can significantly reduce the computational cost while maintaining the simulation accuracy of the target source area.

Although such hybrid strategies have mostly been applied to teleseismic simulations, they are also valuable for regional moderate to strong events (He XH et al., 2019). Examples include the 2021 M_w 6.1 Yangbi earthquake (Zhu GH et al., 2022), the 2022 M_s 6.8 Luding earthquake (Yi GX et al., 2023), and the 2023 M_w 6.0 Jishishan, Gansu earthquake (Hua SB et al., 2024; Wang Q et al., 2024; Yang ZG et al., 2024; Xu TR et al., 2025). These events share features such as shallow source depths, limited rupture areas, and spatially concentrated aftershock sequences typically confined within approximately 50 km from the main earthquake location. Because of the common sparse permanent station distribution (interstation spacing of approximately 50 km), such regional networks can be considered spatially scaled-down analogs of teleseismic monitoring scenarios. The high frequency and shallow source characteristics of regional earthquakes make them very important in hazard assessment (Graves et al., 2011; Wei SJ et al., 2013, 2015; Hejrani et al., 2017; Hejrani and Tkalčić, 2020; Wang X and Zhan ZW, 2020). Although hybrid methods have been applied to regional-scale modeling, they have mainly focused on small local domains around stations (Ba ZN et al., 2025), and few source-region-oriented hybrid modeling studies have been reported to date.

In this study, we propose a full 3D regional-scale hybrid forward simulation method based on the spectral-element method (SEM), tailored for 3D high-frequency waveform modeling (up to 1–2 Hz) under sparse station coverage. The approach separates wave propagation into two parts: a high-accuracy 3D simulation within a near-source excitation subdomain and long-distance wave propagation outside it. The two wavefields are coupled via convolution at a virtual boundary by using the displacement representation theorem (Aki and Richards, 2002). The advantage is that when the source parameters or small-scale structures within the source region are updated, only the low-cost near-source 3D simulation needs to be recomputed. This can significantly reduce the cost of regional-scale waveform modeling with sparse networks. Compared with previous 1D–3D hybrid modeling studies (Wu WB et al., 2018; Qian YY et al., 2024), our method applies the 3D spectral-element scheme to both the source subdomain and the larger outer domain. Additionally, a powerful convolutional perfectly matched layer (CPML) absorbing boundary (Xie ZN et al., 2014) is used in the local subdomain to suppress boundary reflection (Lyu C et al., 2022).

The article is organized as follows: we first introduce the workflow of the hybrid method and validate the method numerically by using a 3D velocity model with topography. Next, we calculate synthetic waveforms by using different regional velocity models and compare them with data from an M_w 5.0 shallow earthquake. We then investigate how the velocity model and frequency content affect waveform fitting. We also use a finite-fault model from Interferometric Synthetic Aperture Radar (InSAR) studies to compute synthetic waveforms and compare them against point-source cases. These results demonstrate the potential of the proposed hybrid method for regional full-3D waveform simulation, source parameter inversion, and rupture imaging.

2. Methodology and Validation

We use the open-source parallel SEM software SPECFEM3D (Komatitsch and Tromp, 1999) to perform all forward simulations presented in this study. The SEM is a high-order finite element method that solves the weak form of the elastic wave equation to simulate seismic wave propagation. It offers high accuracy in handling free-surface topography and complex internal discontinuities. The Cartesian version of SPECFEM3D (SPECFEM3D_Cartesian) is particularly suitable for high-precision simulations of regional-scale seismic wavefields.

2.1 Theory and Workflow

The hybrid simulation method used in this study is based on the displacement representation theorem. Beginning from the elastic wave equation and Gauss's divergence theorem (Wu WB et al., 2018), the wavefield at a given observation point $\boldsymbol{x}$ can be expressed as

$$\begin{aligned} u_n(\boldsymbol{x},t) = \\ + \int_{-\infty}^{+\infty} \mathrm{d}\tau \iint_B G_{in}^{V_2}(\boldsymbol{\xi}, t-\tau; \boldsymbol{x}, 0)\, T_i^{V_1}(u(\boldsymbol{\xi},\tau), \boldsymbol{n})\, \mathrm{d}B(\boldsymbol{\xi}) \\ - \int_{-\infty}^{+\infty} \mathrm{d}\tau \iint_B n_j C_{jipq} \frac{\partial}{\partial \xi_q} G_{pn}^{V_2}(\boldsymbol{\xi}, t-\tau; \boldsymbol{x}, 0)\, u_i^{V_1}(\boldsymbol{\xi},\tau)\, \mathrm{d}B(\boldsymbol{\xi}), \end{aligned} \tag{1}$$

where $T_i^{V_1}(u(\boldsymbol{\xi},\tau), \boldsymbol{n})$ denotes the ith component of the traction vector on the virtual boundary B surrounding computational domain V_1, and $u_i^{V_1}(\boldsymbol{\xi},\tau)$ is the ith component of the displacement at point $\boldsymbol{\xi}$. The expression $G_{in}^{V_2}(\boldsymbol{\xi}, t-\tau; \boldsymbol{x}, 0)$ is the nth component displacement at receiver location $\boldsymbol{x}$ in outer domain V_2, excited by an ith component unit point force applied at point $\boldsymbol{\xi}$ on the virtual boundary. The expression $\frac{\partial}{\partial \xi_q} G_{pn}^{V_2}(\boldsymbol{\xi}, t-\tau; \boldsymbol{x}, 0)$ is the spatial derivative of displacement in the $\boldsymbol{\xi_q}$ direction. In practical implementation, we store time series of traction and displacement vectors computed on the virtual boundary B in domain V_1. In domain V_2, we precompute and store the Green's functions and their spatial derivatives from each boundary point $\boldsymbol{\xi}$ to each receiver position $\boldsymbol{x}$. The synthetic waveforms at $\boldsymbol{x}$ can then be constructed via time-domain convolution by the representation theorem.

Our hybrid simulation workflow consists of three main steps (Figure 1):

Step 1: Source-region wavefield simulation. A small-scale 3D velocity model and source parameters are set in the source region V_1. The wavefield excited by the source is computed within the source region. Three-component displacement waveforms and their spatial derivatives are recorded at all Gauss–Lobatto–Legendre (GLL) points along the virtual boundary B. These recordings form what we refer to as the source-side strain Green's tensor (SSGT).

Step 2: Receiver-side wavefield calculation for the sparse network. Outside the source region, simulations using three-component point forces located at each receiver are performed based on the

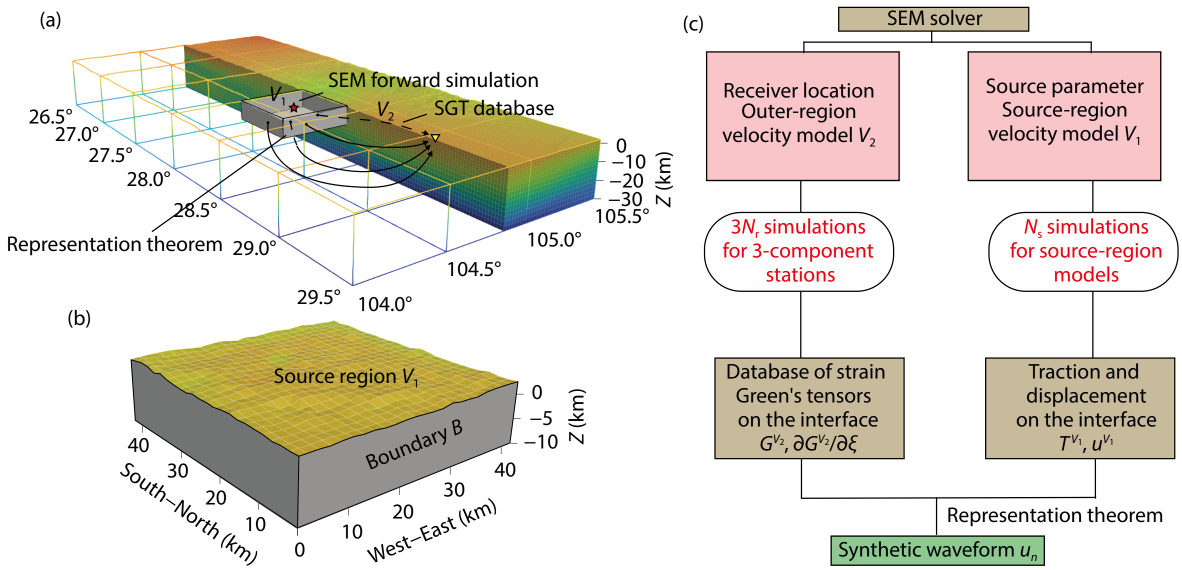

Figure 1. Schematic diagram of the principle and workflow of the regional 3D hybrid method. Panels (a) to (c) illustrate the process of wavefield coupling based on the representation theorem. Panel (a) shows the wavefield simulation from the seismic source to the virtual boundary within a 3D velocity model, along with the construction of the receiver-side strain Green's tensors (RSGT) from the virtual interface to the receiver stations. Panel (b) illustrates the source-region V_1 configuration and virtual interface *B*. When the source-region model is modified, the displacement and stress fields on the five virtual surfaces enclosing the local source area are recomputed and combined with the precomputed RSGT database to achieve accurate hybrid forward modeling of the full wavefield. Panel (c) presents the workflow of the hybrid method: the left part computes the RSGT on the virtual interface *B* based on receiver locations and the outer velocity model in domain V_2. This requires $3N_r$ forward simulations, corresponding to the three-component point-force excitations for each of the N_r receivers. The resulting RSGT database contains the displacement Green's tensors $\boldsymbol{G}^{V_2}$ and their spatial derivatives $\partial \boldsymbol{G}^{V_2}/\partial \boldsymbol{\xi}$ on the interface. The right part simulates the source-side strain Green's tensor (SSGT) on the common virtual interface *B* using the source parameters and the local source-region model in domain V_1. This step require N_s simulations, one for each source-region velocity-model update or source parameter, producing the traction and displacement fields $\boldsymbol{T}^{V_1}$ and $\boldsymbol{u}^{V_1}$ on the interface. These two parts are then integrated via the representation theorem to synthesize the displacement waveforms u_n (n = 1,2, 3) from source to receiver.

reciprocity theorem, and the three-component displacements and their spatial derivatives at all GLL points on the boundary are stored on disk. These form the strain Green's functions (Zhao L et al., 2006) on the boundary, and we refer to the set as the receiver-side strain Green's tensor (RSGT). This step requires $3N_r$ forward simulations, where N_r is the number of receivers. When the large-scale velocity model outside the source region remains unchanged, this step needs to be performed only once.

Step 3: Waveform synthesis based on the representation theorem. The synthetic waveforms are obtained by convolving the SSGT and RSGT databases. This operation is much faster than full 3D simulations. In addition to the wavefield recordings, we precompute and store the integration weights, basis functions, and their derivatives at all GLL points along the boundary elements. The boundary integral in Equation (2) is then evaluated numerically over the virtual surface Γ_b using the standard GLL quadrature formula (Komatitsch and Tromp, 1999):

$$\int_{\Gamma_b} f(x)\,\mathrm{d}^2x = \int_{-1}^{1}\int_{-1}^{1} f(x(\xi,\eta))\,J_b(\xi,\eta)\,\mathrm{d}\xi\mathrm{d}\eta \approx \sum_{\alpha,\beta=0}^{n_l} \omega_\alpha\omega_\beta f^{\alpha\beta} J_b^{\alpha\beta}, \tag{2}$$

where $\omega_\alpha, \alpha = 0, 1, \ldots, n_l$ are the integration weights associated with the n_l-order GLL points, $J_b^{\alpha\beta} = J_b(\xi_\alpha, \eta_\beta)$ is the Jacobian determinant at point $x(\xi_\alpha, \eta_\beta)$, and $f(x(\xi,\eta))$ represents the integrand, which in this case corresponds to the convolved wavefield $u_n(\boldsymbol{x}, t)$ computed at each boundary point.

2.2 Validation Test

To validate the proposed hybrid method, we use the M_w 5.0 earthquake that occurred on January 3, 2019, in Gongxian, Sichuan Province, located in the south of the Sichuan Basin. Source mechanism solutions derived from local sparse seismic network data (Lei XL et al., 2019a, b; Yi GX et al., 2019) and fault models obtained from InSAR observations (Luo H et al., 2022; Wang S et al., 2022) both indicate that this event occurred at a shallow depth of less than 2 km. The point-source moment tensor is taken from the Global Centroid Moment Tensor (GCMT) catalog, with a fixed source depth of 2 km (Yi GX et al., 2019).

We utilize the SWChina-V2.0 model (Liu Y et al., 2023; referred to as CVM3D) for the large-scale velocity model outside the source region. Within the source region, a higher resolution local tomographic velocity model for the Changning–Xingwen region (CX; Tian W et al., 2024) is embedded as a changed source-region velocity structure. The local model is smoothly merged with the large-scale regional model by using a taper function (Zang C et al., 2024), ensuring the continuity of both velocity models. We compute three-component synthetic wavefields for a set of sparse local stations by using both full 3D SEM modeling and the hybrid SEM method proposed in this study. The dataset includes 18 broadband stations from the Sichuan regional seismic network within the target area. The large-scale SEM simulation domain covers 160 × 330 × 30 km (E–N–Z) and is discretized into 160 × 300 × 33 spectral elements with an average size of 1 km. With this mesh and the CVM3D velocity (V_s > 2 km/s), the minimum resolvable period is approximately 0.5 s. A 5-km-thick CPML absorbing boundary is applied at the mesh edges. The total simulation time is 100 s, with a 0.01 s time step. One run used 240 CPU core-hours. The virtual boundary of the source region spans from approximately 104.7° to 105.1° longitude and 28.0° to 28.4° latitude, with a bottom depth of 10 km. Within this region, we use the local 3D tomographic model for Changning, covering 60 × 60 × 20 km (E–N–Z). The model is discretized into 60 × 60 × 23 spectral elements, and it set a 5-km-thick CPML absorbing boundary. The size of the virtual boundary is 45 × 45 × 10 km, which is smaller than the modeling, to avoid including points within the absorbing boundary. The total simulation time is 30 s for the source-region wavefield to ensure that the complete wavefield propagates out of the virtual boundary. The SSGT and RSGT databases share the same virtual boundary and time step.

In our hybrid method, we utilize full integration over all 25 GLL points by using a Gaussian source-time function with a half-duration of 0.25 s, corresponding to a dominant frequency of approximately 2 Hz. The hybrid synthetic waveforms of all 18 stations (Figure 2a) closely match the direct SEM results, with amplitude differences of 1%–2% (see figure in Section 4.1). The localized source-region simulations that produce the SSGT require only approximately 2 CPU core-hours (T^{V_1}) each, whereas a full direct SEM forward simulation requires roughly 240 CPU core-hours in domain V_2 (T^{V_2}). However, constructing the receiver-side strain Green's tensors (RSGT) for all stations (N_r) requires a one-time set of large-scale SEM simulations: each simulation consumes approximately 240 CPU core-hours (T^{V_2}), and $3N_r$ simulations are needed to account for the three components, resulting in an initial computational cost of $T^{V_2} \times 3N_r$ CPU core-hours (Table 1). Because the RSGT construction represents a substantial one-time expense,

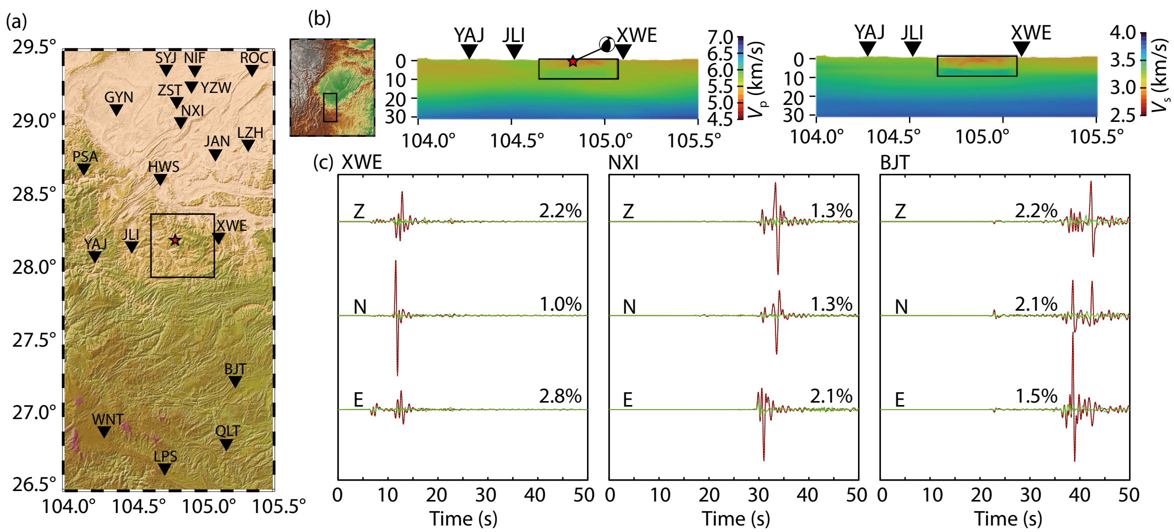

Figure 2. (a) Topography of the study area, the distribution of broadband permanent stations (black triangles), and the earthquake epicenter (red star). The black box indicates the small region used for our hybrid simulation. The black box in the upper right corner of the illustration shows the location of the study area in the Sichuan–Yunnan region. (b) Vertical cross sections of V_p and V_s. The north–south profile is along 104.85°E, and the east–west profile is along 28.21°N. The local source region (black box), measuring 45 × 45 × 10 km, is modeled using the Changning–Xingwen (CX) velocity model. (c) Validation of forward simulation using the CVM3D model combined with the CX local model. The point-source moment tensor is a high-angle reverse fault with strike 350.6°, dip 55.1°, and rake 39.7°. A Gaussian source time function with a half duration of 0.25 s is used to generate a high-frequency velocity waveform. The black lines represent waveforms from direct SEM simulation; the dashed red lines are waveforms synthesized by the 3D hybrid method using 25 GLL point integrations; the green lines show the residuals between the direct and hybrid method waveforms, amplified by a factor of 10. The numbers to the right of each waveform indicate the maximum residual difference between the synthetic waveform obtained by the hybrid method and the waveform from direct simulation. Hybrid-method synthetic waveforms for the other stations are shown in the figure in Section 4.1.

Table 1. Comparison of computational costs between the direct 3D SEM and the hybrid 3D SEM methods.[a]

Cost or requirement	Direct 3D SEM	Hybrid 3D SEM
Storage requirement	—	$3N_r + N_s$
Number of simulations	N_s	$N_s + 3N_r$
CPU cost	$T^{V_2} \times N_s$	$T^{V_2} \times 3N_r + T^{V_1} \times N_s$

[a] N_s, number of regional velocity models in V_1; N_r, number of receiver stations in V_2; T^{V_1}, CPU time for one source-region SEM simulation (2 core-hours in this case); T^{V_2}, CPU time for one large-scale SEM simulation (240 core-hours in this case).

the overall efficiency gain of the hybrid method depends on the number of source-region model updates or source variations (N_s). The method becomes truly advantageous only when this change in source region greatly exceeds the number of stations, such that $T^{V_2} \times N_s > T^{V_2} \times 3N_r + T^{V_1} \times N_s$.

3. Influence of the Velocity Model and Source Parameters

Shallow velocity structures play a critical role in the propagation of seismic waves from shallow earthquakes and the simulation of strong ground motion. Near-surface low-velocity layers tend to trap energy (Berg et al., 2021), asymmetrically amplify near-fault ground shaking (Yang HF, 2015), and enhance surface waves. Moreover, if a low-velocity sedimentary layer surrounds the source, the resulting time delays may lead to overestimation of the source depth with an inaccurate velocity model (Neves et al., 2024). Most real-time event catalogs rely on local 1D velocity models; however, under complex underground conditions, such models may introduce significant location errors. The Changning–Xingwen region, situated at the southern margin of the Sichuan Basin and serving as an important shale gas extraction zone, provides a typical case to investigate the shallow crustal structure (≤5 km) and its relevance to both induced earthquakes and regional tectonics (Yang W et al., 2021).

3.1 Overview of the Velocity Models

We select a series of 3D local velocity models for waveform modeling and comparison with observations. For the small-scale source-region modeling, four models are tested: (1) the portion of the SWChina-V2.0 model (CVM3D-V2.0; Liu Y et al., 2023) covering the source area, (2) a high-resolution shear-wave velocity model for Changning (LiuVs; Liu QX et al., 2023), (3) a tomographic model of the Changning–Xingwen region (CX; Tian W et al., 2024), and (4) a modified local 1D model (Modified1D). For the large-scale outer region in the hybrid method, we test both the CVM3D-V2.0 and China Seismic Experimental Site (CSES)-VM1.0 (Wu JP et al., 2024) models.

The datasets for inversion and resolution of these models are briefly described as follows. The CVM3D-V2.0 is a 3D velocity model for southwestern China based on more than 40,000 local earthquake and ambient noise cross-correlation observations, with a near-surface resolution of approximately 2.5 km. In contrast to the CVM3D-V2.0, CSES-VM1.0 achieves a vertical resolution of 2–5 km in the upper crust, clearly imaging low-velocity sedimentary layers within the Sichuan Basin. For the source region, the LiuVs model (from Liu QX et al., 2023) is constructed using 3D ambient noise tomography with a dense temporary array and permanent stations. It resolves the shear-wave velocity structure from 0 to 8 km depth, with a lateral and vertical resolution of 7.5 km and 0.5 km, respectively. We extend it to a P-wave velocity model using a local reference V_p/V_s = 1.73, which corresponds to the typical Poisson's ratio of the upper crust (Brocher, 2005; Lei XL et al., 2017), and merge it smoothly below 8 km into CVM3D. The CX model (Tian W et al., 2024) uses double-difference body-wave tomography based on a dense array (approximately 4.5 km spacing), resolving the top 8 km with a 2/0.5 km (horizontal/vertical) resolution, also merging into the CVM3D at depth. The LiuVs model exhibits the lowest V_s above 2 km, with a strong vertical gradient above 5 km. In contrast, the CX model has faster velocities above 5 km and more pronounced small-scale lateral variations. As a reference, we construct a Modified1D velocity model based on the local geological conditions and regional adaptations of Zeng Q et al. (2020). This model features the lowest V_p and V_s above 3 km, with a sharp velocity contrast at approximately 4 km depth (Figure 3a) and with a vertical resolution of less than 1 km. In summary, the four models are similar below 5 km but have significant differences above 5 km: the LiuVs and Modified1D models have lower speeds, whereas the CX and CVM3D have relatively faster speeds.

3.2 Influence of Source-Region Velocity

To assess how source-region velocity models affect the waveform, we use the hybrid method with a fixed outer region (CVM3D) and replace only the local velocity structure. For stations within 70 km, body-wave phases (P, S) and surface waves are difficult to separate in the long-period bands, so we compare the full waveforms directly. For stations beyond 70 km, we manually pick arrival times for the P and S phases and selected time windows: 10 s before and two maximum filter periods after the P onset, and 10 s before to 40 s after the S-wave onset. All three-component records were rotated into tangential (T), radial (R), and vertical (Z) components, then bandpass-filtered using the same frequency bands. Normalized cross-correlation measurements were performed to quantify the similarity between synthetic waveforms and observed data (Figure 4).

For station XWE (located 32 km due east of the epicenter; Figure

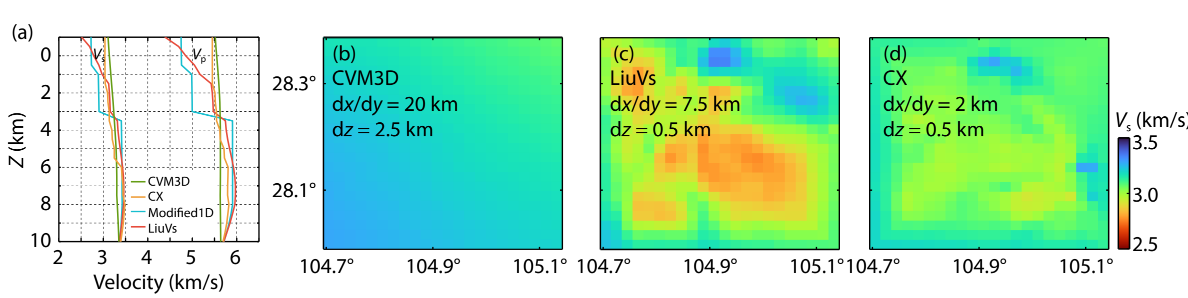

Figure 3. (a) Comparison of depth-averaged velocity profiles for four velocity models within the local source region. The regional models are merged into the CVM3D below 8 km. (b–d) Horizontal slices showing the depth-averaged V_s within the upper 5 km for the (b) CVM3D, (c) LiuVs, and (d) CX models. Here, dx/dy denotes the horizontal resolution and dz denotes the vertical (depth) resolution of each model. All velocity models in (b) to (d) share the same color scale, as indicated on the right.

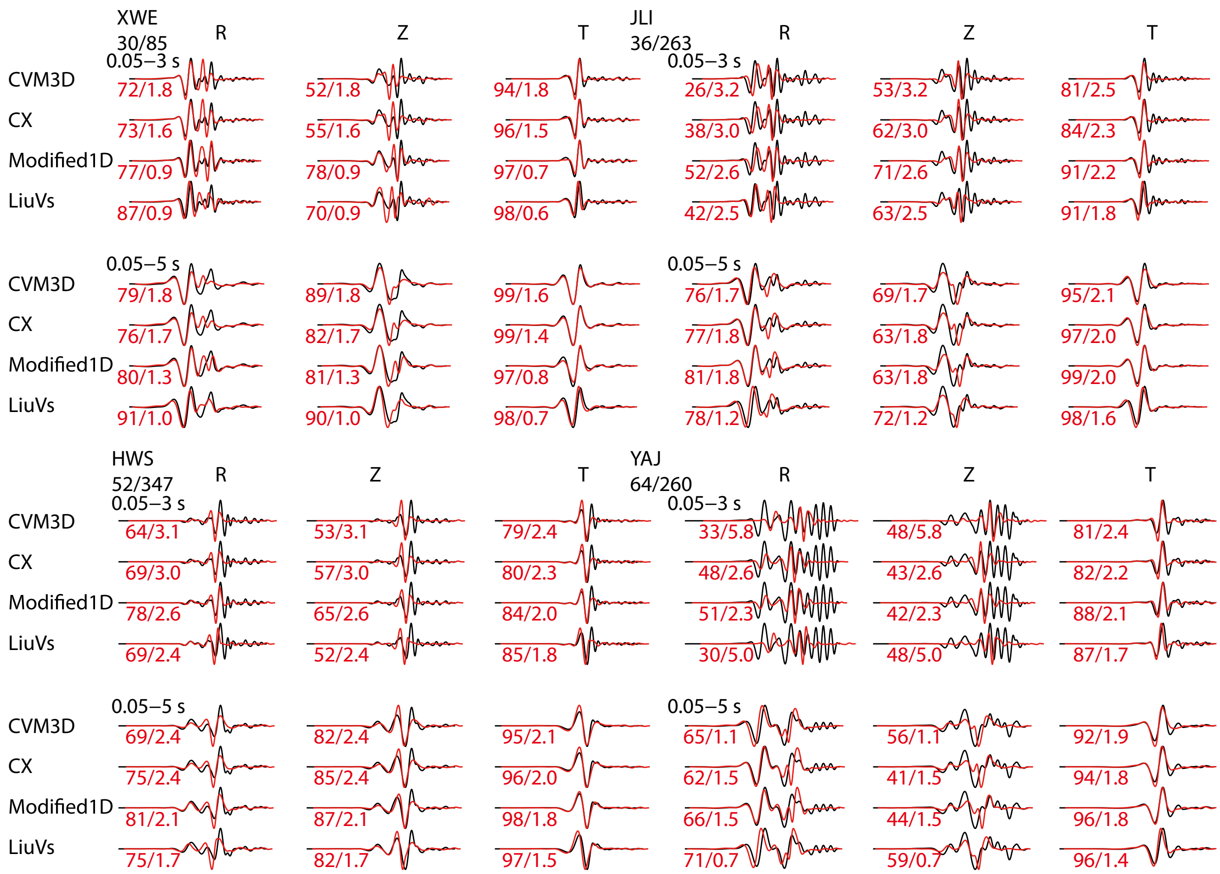

Figure 4. Comparison between synthetic velocity waveforms (in red) and observed waveforms (in black) at four near-field stations (XWE, JLI, HWS, and YAJ) in the 20–5 s and 20–3 s frequency bands for four local velocity models. The models, from top to bottom, are the CVM3D, CX, Modified1D, and LiuVs models. Panels (a)–(d) correspond to waveform fits for stations XWE, JLI, HWS, and YAJ, respectively. Below each waveform pair, the cross-correlation travel-time shift (in seconds) and NCC coefficient (in %) between observed and synthetic waveforms are labeled. The numbers shown beneath each station name indicate the epicentral distance and azimuth. Station locations are shown in Figure 2.

4), the seismic wave propagates mainly in the source region. All models performed similarly in the 20–5 s frequency band. In the 20–3 s frequency band, the LiuVs and Modified1D models provided better fits in the R and Z components, whereas the CX and CVM3D showed slightly higher time delays. All models showed good fits for the T component. For the T component, all models performed well in the 20–5 s and 20–3 s frequency bands. In contrast, station JLI (located 33 km west of the epicenter) showed good fits in the 20–5 s frequency band but significant misfits at high frequency in the coda, indicating strong lateral heterogeneity in the shallow structure. For station HWS (52 km north), where part of the path travels through the outer model, all models performed reasonably well in the 20–5 s frequency band (normalized cross-correlation [NCC] > 60%). In the 20–3 s frequency band, the Modified1D had the highest NCC for the R and Z components. At station YAJ (62 km west), the low-frequency waveform fit was poorer, and the strong Rayleigh wave train could not be reproduced well by any source model.

For distant stations, the Modified1D model consistently fit better than the other models at all frequencies. In the 20–5 s frequency band, all models exhibited similar results (Figure 5a). However, in the 20–3 s frequency band (Figure 5b), the Modified1D yielded the highest NCC value, indicating the importance of an accurate shallow structure in the source region for waveform fitting. Overall, theoretical waveforms differed by less than 10% in both shape and arrival times, indicating that the waveforms at distant stations were mainly affected by the outer large model. In the following section, we compare two 3D models for the outer region.

3.3 Influence of Large-Scale Velocity Modeling

As discussed in the previous section, we find that the Modified1D velocity model within the source region provides a good fit in the high-frequency band. We then test the CVM3D and CSES models outside the source region combined with the Modified1D model (Figure 6).

As in Section 3.2, we first compare synthetic and observed waveforms at four stations within 70 km (Figure 7). All stations have similar results in the 20–5 s frequency band. Although the outer model contributes only a small portion of the propagation path from the source to these near stations, modifying the outer model still improves the waveform fit. For example, at station JLI, time delays in the 20–3 s frequency bands are slightly reduced when using the CSES model. For stations HWS and YAJ, the CSES model provides better fits in the R and T components.

For stations beyond 70 km (Figure 8), in the 20–5 s frequency band, time residuals and NCC values from the CVM3D and CSES are generally similar. For southern stations LPS and WNT, the

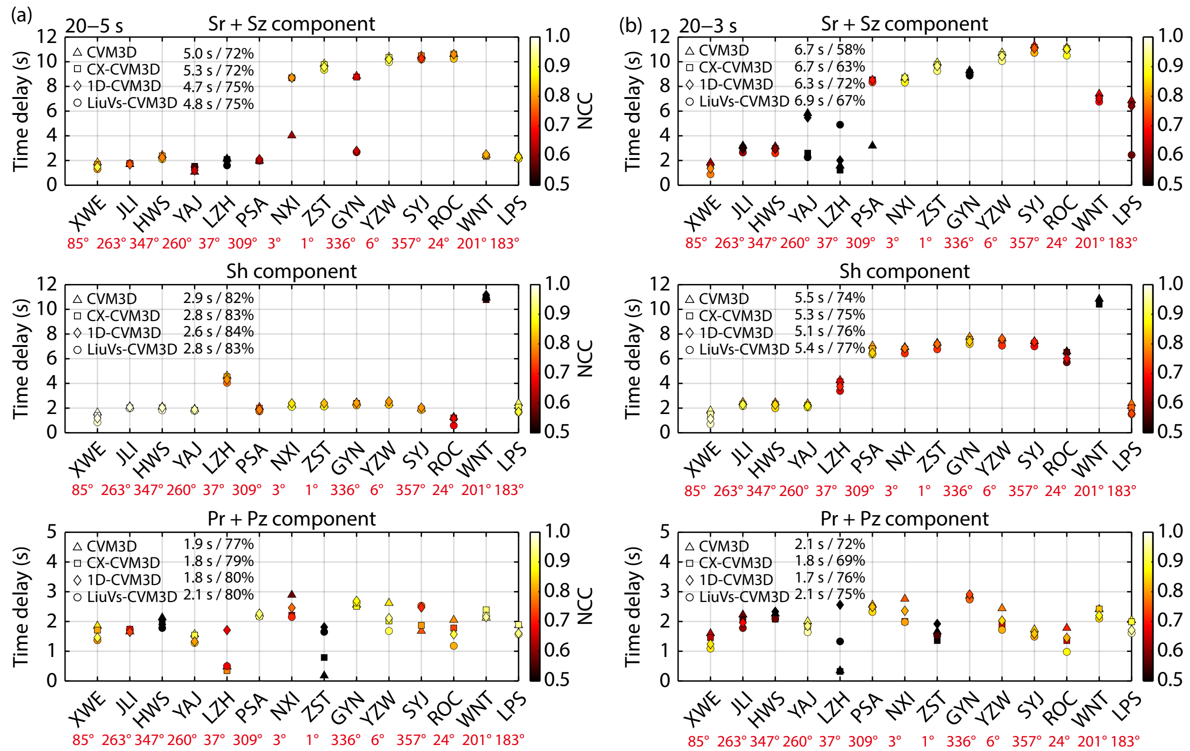

Figure 5. Comparison of NCC values and travel-time residuals for the Sr + Sz, Sh, and Pr + Pz components. Panels (a) and (b) show results in the 20–5 s and 20–3 s frequency bands, respectively. The triangles denote results from the CVM3D model, the squares denote those from the CX-CVM3D model, the diamonds denote those from the 1D-CVM3D model, and the circles denote those from the LiuVs-CVM3D model. The vertical axis represents the travel-time residuals (s), and the horizontal axis lists the seismic stations ordered by epicentral distance. The symbol colors correspond to the NCC values, with warmer colors indicating higher correlations (see the color bar). Azimuths are marked below the station name. For each velocity model, the average waveform-based NCC values and time delay are annotated on the figure.

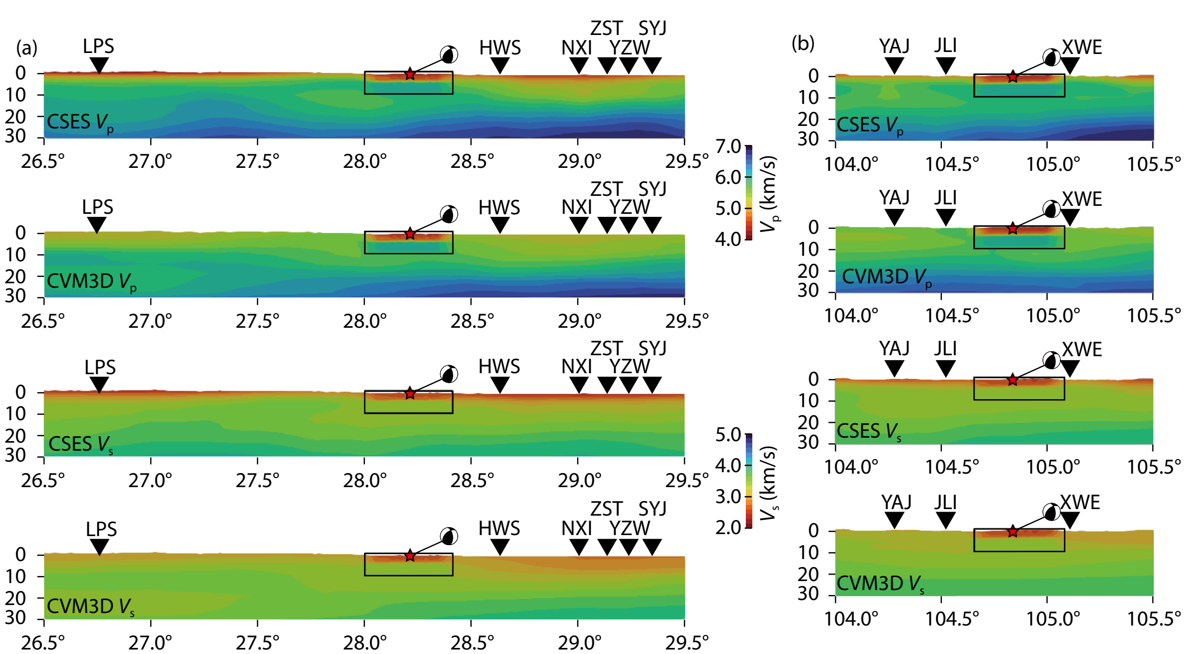

Figure 6. Vertical profiles of V_p and V_s velocity models from the CVM3D and CSES, along with slice locations. (a) North–south profile across the epicenter. (b) East–west profile through the epicenter. The north–south profile is located at 104.85°E, and the east–west profile at 28.21°N. The black box indicates the embedded Modified1D velocity model in the source region, covering an area of 45 × 45 × 10 km.

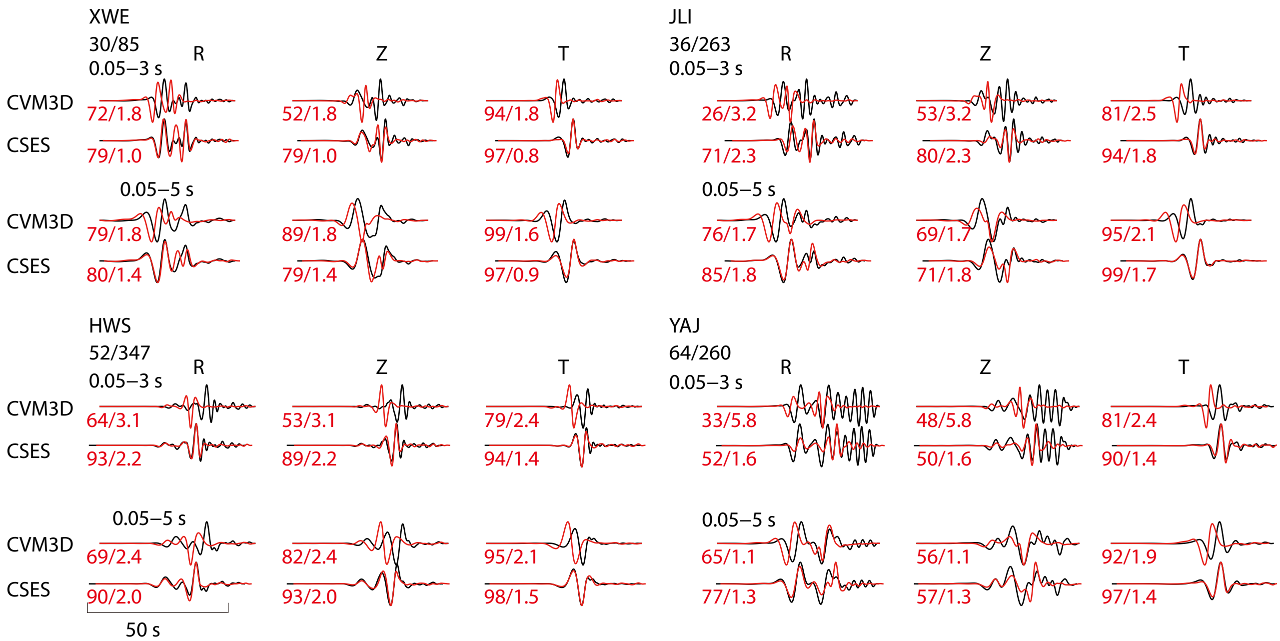

Figure 7. Comparison of synthetic waveforms (red) generated using the Modified1D model combined with the CVM3D and CSES models, and observed waveforms (black) at four stations (XWE, JLI, HWS, and YAJ) in the 20–5 s and 20–3 s frequency bands. Cross-correlation travel-time shifts (in seconds) and NCC values (in %) are indicated in the lower left corner of each waveform pair. The epicentral distance and azimuth are noted beneath each station name; station locations are shown in Figure 2.

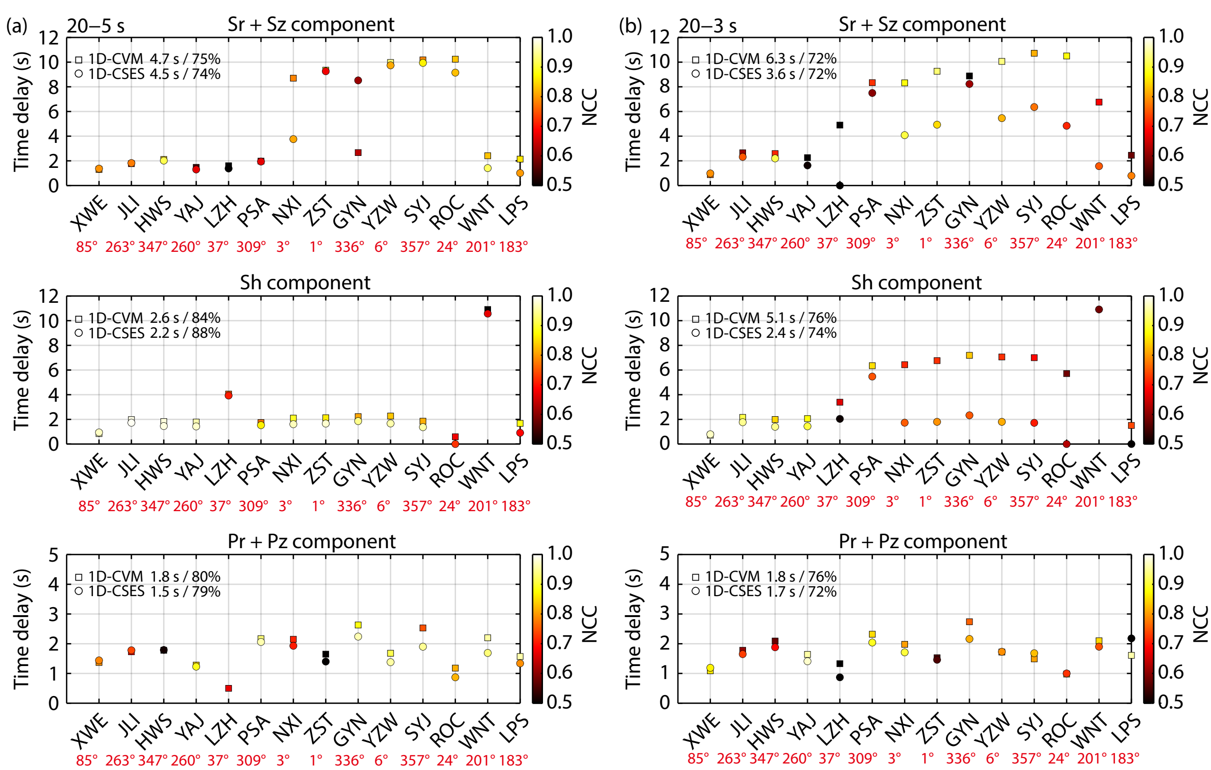

Figure 8. Comparison of NCC values and travel-time residuals for the Sr + Sz, Sh, and Pr + Pz components. Panels (a) and (b) show results in the 20–5 s and 20–3 s frequency bands, respectively. Squares denote results from the 1D-CVM3D model, whereas circles denote results from the 1D-CSES model. The vertical axis represents the travel-time residuals (s), and the horizontal axis lists seismic stations ordered by epicentral distance. The symbol colors correspond to the NCC values, with warmer colors indicating a higher correlation (see color bar). For each velocity model, the average waveform-based NCC values and time delay are annotated on the figure.

surface wave is well-fitted and shows a low time delay. For northern distant stations, time residuals of Love waves are generally less than 2 s, whereas Rayleigh waves on the R and Z components show higher time delays. In the 20–3 s frequency band, the CSES model yields lower time delays than the CVM3D for surface waves. The NCC values of both models are higher than 70% in the 20–3 s frequency band, and the CVM3D model has a higher value. For P-waves, both the CVM3D and CSES provide an NCC > 70% and the CVM3D provides a higher NCC value.

In summary, the waveforms of the two models are relatively close, and both fit the data well (NCC > 70%) in the 20–5 s frequency band, corresponding to their similar velocities in the upper crust. In the 20–3 s frequency band, both models have good fit to the waveform (NCC > 70%) for most stations. Substantial arrival-time delays are concentrated in the north of the Changning area (Tan YY et al., 2023), and the CSES model predicts a lower time delay in the Sichuan Basin.

3.4 Comparison Between Point-Source and Finite-Fault Modeling

In source studies, the source is commonly represented by using either a point-source model or a finite-fault model. Point sources are well-suited for modeling long-period seismic waves under appropriate assumptions, and they are widely used in rapid moment tensor inversions and preliminary magnitude estimates. However, point-source models neglect the geometric complexity of the fault, as well as the nonuniform slip distribution and directivity effects during rupture propagation. As a result, they often introduce significant inaccuracies in near-field ground motion simulations and for large-scale rupture events (Lay et al., 2018). In contrast, finite-fault models incorporate the spatiotemporal distribution of slip on the complicated fault plane, which can better characterize the rupture initiation, termination, and propagation complexity (Hsieh et al., 2016).

Here, we use the Modified1D-CSES hybrid 3D velocity model to simulate synthetic waveforms from both the point-source and

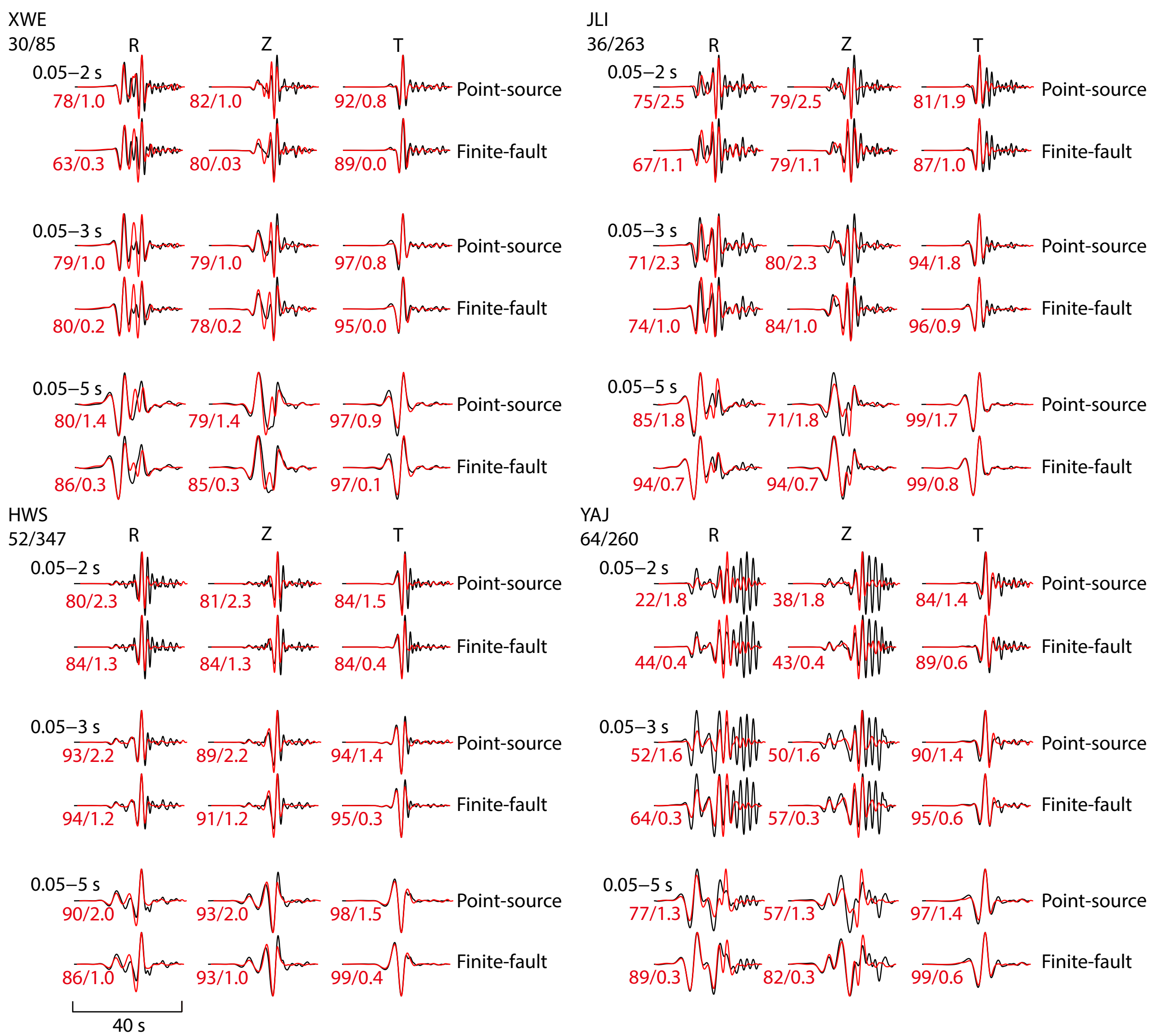

Figure 9. Waveform comparison at four stations with epicentral distances of less than 70 km. Velocity waveforms of the R, Z, and T components from the Modified1D-CSES hybrid velocity model are shown for both the point source and finite-fault models in the 20–3 s and 20–5 s frequency bands. Synthetic waveforms are shown in red, and observed waveforms are shown in black.

finite-fault models and compare them with observed data (Figure 9). The finite-fault source model is derived from InSAR inversion by Wang S et al. (2022). The finite-fault rupture initiation time is set equal to the point-source origin time.

For stations within 70 km, the arrival-time differences between P- and S-waves are larger in the finite-fault simulations and more closely match the observed data. In contrast, the S-waves in the point-source simulations arrive too early. The finite-fault simulation exhibits clearer rupture directivity (Figure 10). The finite-fault model improves waveform matches for stations not aligned with the main rupture direction, such as XWE, JLI, and YAJ (Figure 9). In the point-source simulations, the P-coda amplitude is underestimated. The finite-fault model yields larger amplitudes, which are more consistent with observations. Moreover, the finite-fault simulations produce richer waveform details, improving the agreement with recorded data in the P-coda. For stations in the rupture direction (e.g., HWS), both source models perform similarly and yield good fits to the observations (Figure 9). At stations beyond 70 km, the improvements from the finite-fault model are in the P-wave window, particularly in the 20–3 s frequency band (Table 2). However, for surface waves in different frequency bands, the finite-fault model does not significantly improve waveform fits. The shallow structure along the path dominates the waveform characteristics, while the influence of source complexity is minor (Graves and Wald, 2001).

4. Discussion

4.1 Hybrid Simulation Method and Its Improvements

In our hybrid method, we compare two spatial quadrature schemes: a low-resolution approach that uses only the face-center point and face area per spectral element, and a high-resolution

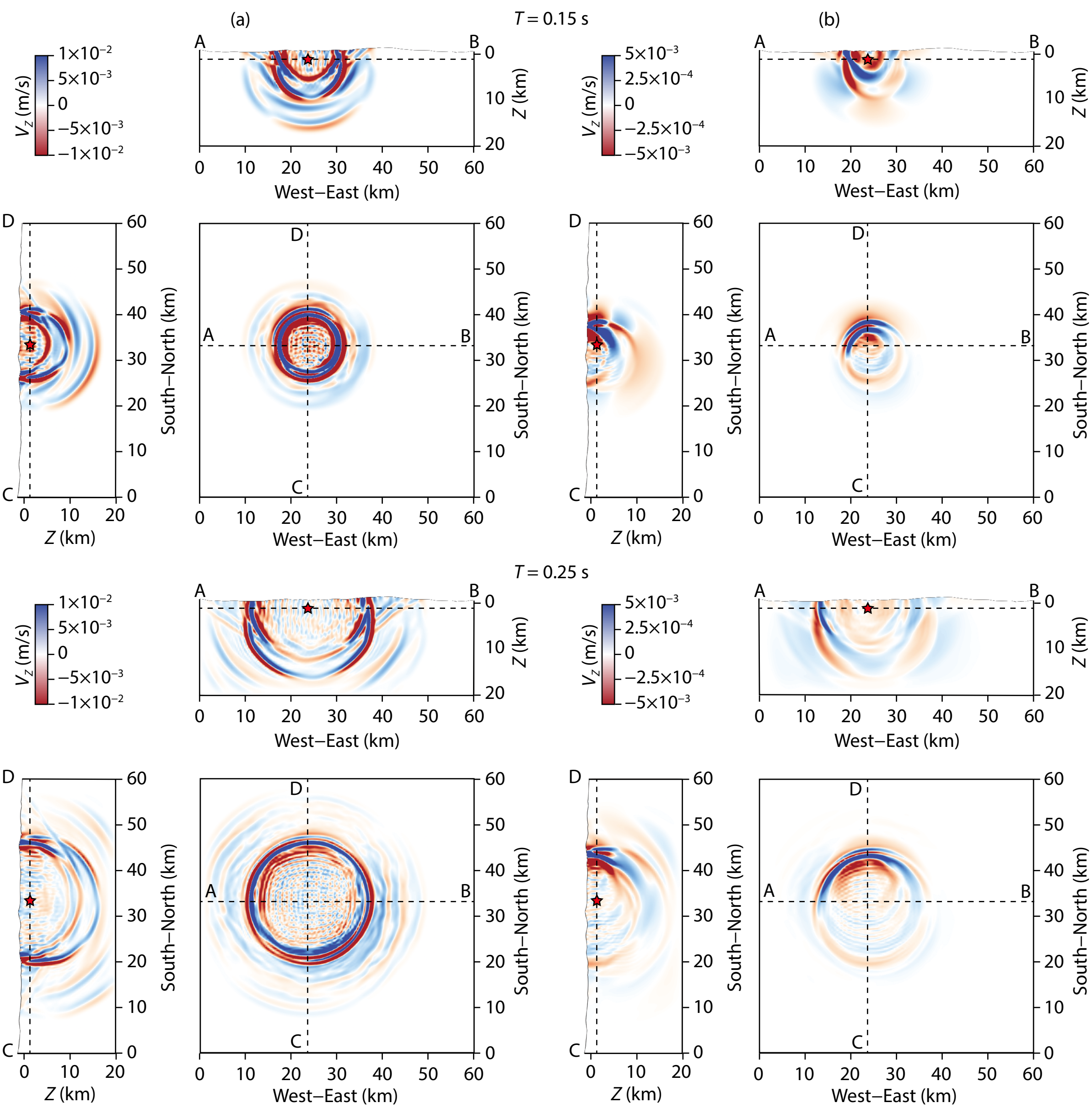

Figure 10. Snapshots of excited wavefields for the point-source model (a) and the finite rupture model (b). The wavefield from the finite rupture model highlights a much stronger source rupture directivity effect, with rupture propagating toward the northwest.

Table 2. Mean travel-time residual (s) and NCC (%) for point-source and finite-fault models in the 20–5 s and 20–3 s bands.

Frequency band	Sr + Sz	Sh	Pr + Pz
20–5 s			
Point-source	4.5/74	2.2/88	1.5/79
Finite-fault	3.6/78	0.9/86	0.3/79
20–3 s			
Point-source	3.6/72	2.4/74	1.7/72
Finite-fault	3.2/76	1.9/74	0.8/75

approach that integrates over all 25 GLL points with their quadrature weights. We evaluate both using sources with half-widths of 0.25 s and 0.5 s (dominant frequencies of 2 Hz and 1 Hz, respectively; see Figure 11).

At 2 Hz, the single-point integration markedly increases modeling errors in the S-wave and surface-wave coda: high-frequency surface-scattered energy in the S-wave and surface-wave arrivals is poorly synthesized. By contrast, first-arrival body-wave phases are only slightly affected because their dominant frequency is lower and their propagation path is downward, away from the free surface. Topography-induced mesh distortion and free-surface reflections or interference further heighten the sensitivity of near-surface wavefields to integration accuracy. At 1 Hz, the single-point scheme yields only slight errors; the full waveform, including surface-scattered waves, remains close to the 25-point result.

Accordingly, high-resolution integration is essential for scattered-wave analysis and high-frequency surface-wave studies, especially the high-frequency coda waves sensitive to shallow structure and topography (Masson et al., 2014; Wu WB et al., 2018; Wang N et al., 2019). For low-frequency simulations that do not approach the resolution limit of the grid (e.g., 1 Hz), the center-point low-resolution integration is an efficient choice: the error is negligible for location and inversion based on phase arrivals and waveform cross-correlation while reducing storage and computational costs by a factor of 25.

When strong heterogeneities exist outside the source region, the first-order scattered waves that travel directly from these heterogeneities to stations can be accurately recovered. In contrast, waves that are reflected or scattered by external heterogeneities reenter the source region and are then reflected again toward the stations corresponding to second-order scattering, which cannot be modeled in the current hybrid simulation. All outgoing scattered waves are absorbed by the boundary conditions and do not reenter the computational domain. Thus, only first-order scattering can be considered (Masson et al., 2014; Lyu C et al., 2022, 2025). Because of geometric spreading and intrinsic attenuation, the

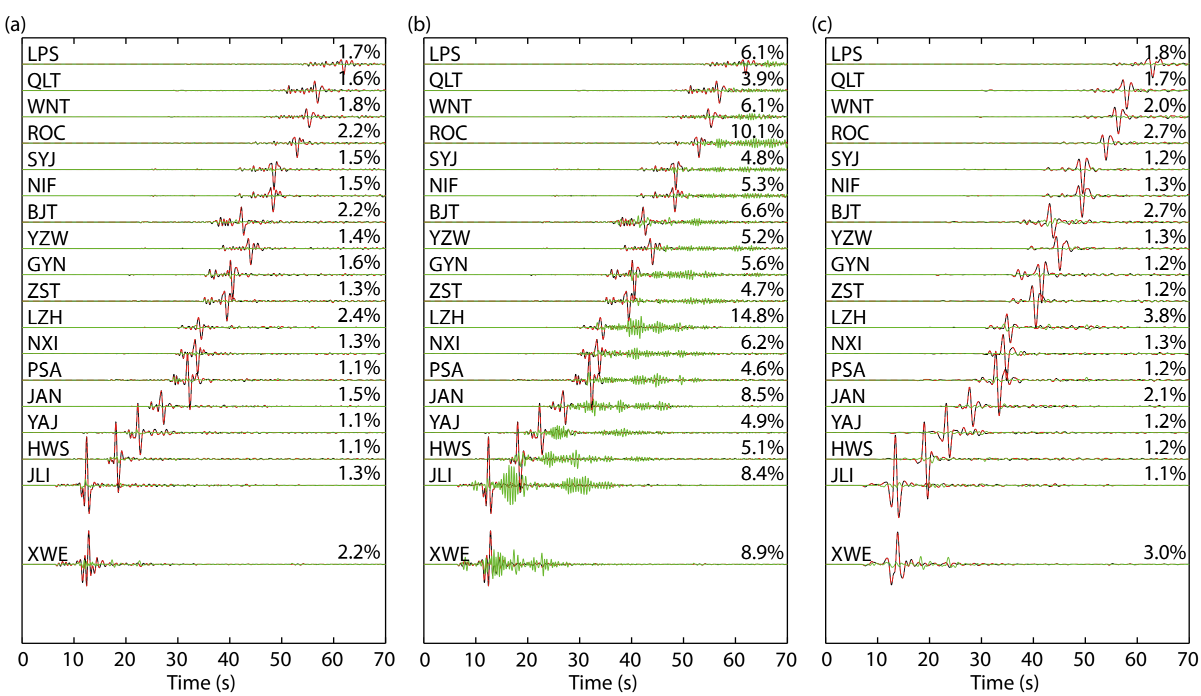

Figure 11. Z-component velocity integrated using only the center point or all 25 points. (a) 2 Hz waveforms integrated using all 25 GLL points. (b) 2 Hz waveforms integrated using only the center point. (c) 1 Hz waveforms integrated using only the center point. The black lines represent waveforms from direct SEM; the dashed red lines are waveforms synthesized by the 3D hybrid method. The green lines show the residuals between the direct and hybrid method waveforms, amplified by a factor of 10.

energy of second-order scattering is much weaker than that of the direct and first-order scattered waves, which dominate the imaging process. According to the Born approximation (Zhao L et al., 2000; Liu Q and Gu YJ, 2012), both velocity-model and source-parameter inversions account for only first-order scattering and neglect multiple scattering from small-scale heterogeneities. When strong external heterogeneities, such as the Moho discontinuity (Zang C et al., 2024) or subduction interfaces (Monteiller et al., 2013), are present, these structures should be included in the regional model to simulate the multiple scattering.

Traditional absorbing boundary conditions (Clayton and Engquist, 1977; Stacey, 1988) are based on paraxial approximations to the scalar or elastic wave equations and exhibit reduced absorption efficiency for grazing-incidence waves. Moreover, because the damping parameters are fixed, the amplitude of reflected waves tends to increase with frequency (Xie ZN et al., 2014). In contrast, the CPML absorbing layer provides much higher efficiency for grazing-incidence waves, and its frequency-dependent damping terms ensure robust absorption across a broad frequency band (Xie ZN et al., 2014, 2016; Liu YS et al., 2019). Numerical experiments by Xie ZN et al. (2014, 2016) demonstrated that a CPML thickness of about one minimum wavelength is sufficient to achieve excellent absorption, with a reflection coefficient of approximately 10^{-3}. This high absorption efficiency enables the use of a relatively small source region without enlarging the computational domain to suppress reflections, thereby ensuring waveform accuracy while significantly improving computational efficiency.

4.2 Shallow Structure Beneath Changning

Previous studies have revealed significant 3D velocity variations in the crust within the uppermost 10 km beneath the Changning region (Wang MM et al., 2016; Long F et al., 2020; Tan YY et al., 2020; Zuo KZ et al., 2020; Li DH et al., 2021), as well as pronounced low-velocity anomalies in the upper 3 km (Zhou PC et al., 2021; Liu QX et al., 2023). Travel-time tomography using dense arrays also indicates high V_p/V_s ratios in the shallow subsurface of this region (Tian W et al., 2024). Receiver-function imaging (Tang CX et al., 2022) and joint inversion of P-wave polarization and surface waves (Xiao X et al., 2021, 2024) suggest that shallow-crustal S-wave velocities in the western Sichuan Basin can be as low as 2.4 km/s, with sediment thicknesses possibly exceeding 5 km. Ambient-noise tomography in Weiyuan, a shale-gas field in the south-central basin, shows low S-wave velocities: 2.2–2.7 km/s in the upper 2 km and 2.3–2.8 km/s at 3–5 km depth (Zeng Q et al., 2020).

The waveform comparisons in Section 3.2 indicate that models with lower near-surface velocities in the source region (e.g., Modified1D, LiuVs) yield systematically higher waveform similarity—especially for the P-coda in the 3–20 s frequency band. Because the P-coda is highly sensitive to source depth (He XH et al., 2019; Wang N et al., 2019; Noe et al., 2024), this pattern is consistent with the low-velocity characteristics produced by shallow sedimentation in the Changning area (Ma ST, 2010). Strong coda scattering and long Rayleigh-wave trains at western stations further indicate pronounced lateral inhomogeneity. For distant stations, the Modified1D model consistently fits better than the other models across all frequencies.

Although our tests do not uniquely determine layer thicknesses or vertical gradients, they favor slower velocities above 3–5 km depth and highlight strong lateral heterogeneity at scales of a few tens of kilometers. Our results support the presence of a strong low-velocity sedimentary layer in Changning (Sheng MH et al., 2020, 2022; Tan YY et al., 2023; Tian W et al., 2024), which may increase the seismic hazard in the region (Lei XL et al., 2019a, b).

4.3 Influence of the Large-Scale Velocity Model

For large-scale tests, results show a significant velocity reduction within the Sichuan Basin, located in the northern part of the study area. Our cross-correlation measurements of 20–3 s surface waves support this lateral heterogeneity, with substantial arrival-time delays concentrated in the northern stations. The CSES model features lower velocities in the upper 5 km of the northern Sichuan Basin, and it provides better surface-wave fits at northern stations in the 20–3 s high-frequency band compared with CVM3D. This may be because the CSES velocity model inverted more observational data within the Sichuan Basin and uses receiver function joint inversion, which is more sensitive to shallow sediments. This result highlights the importance of lateral heterogeneity and shallow velocity accuracy in 3D modeling. Rayleigh-wave residuals are notably larger than Love-wave residuals in the 20–5 s and 20–3 s frequency bands, indicating that the current resolution of P- and S-wave velocities in the shallow crust needs improvement, especially within the sedimentary layers of the Sichuan Basin. Previous studies (Li HY et al., 2009; Wei ZG et al., 2020) have reported that S-wave velocities shallower than 3 km in the Sichuan Basin are generally below 3 km/s. Geological modeling results by Wang MM et al. (2016) showed P-wave velocities below 5 km/s down to 5 km depth. The Sichuan Basin may have even lower velocities than those represented in the models, and the velocities of both the CSES and CVM3D models are higher than the shallow velocity in this area, suggesting that further refinement for shallow structures is necessary to improve waveform simulation accuracy.

Comparison between two large-scale models indicates that more accurate shallow velocity models improve high-frequency waveform fits and, consequently, enhance depth and location accuracy in earthquake source studies (Guo XQ et al., 2024). Several studies have shown that resolving shallow velocity models requires the use of denser arrays, higher frequency data, and more suitable inversion methods for shallow velocity structures (Li C et al., 2020; Shao XH et al., 2022; Ni HY et al., 2025a, b). Wang X et al. (2024) proposed a hybrid model, ShallowVs_hyb, for the Sichuan–Yunnan region, which merges the shallow-layer structure from the China seismological reference model (Xiao X et al., 2024) with the deep crustal structure of CVM3D-V2.0. Synthetic waveforms based on ShallowVs_hyb match observed data more accurately, especially the surface wave. Notably, the only difference of this model from CVM3D-V2.0 lies in the structure above 15 km depth, highlighting the importance of modeling shallow velocity structures in waveform simulation. Small-scale shallow structures within the Sichuan Basin may require waveform inversion based on high-frequency data and dense array observations (Yao HJ, 2020; Wang X et al., 2024).

4.4 Influence of the Finite-Fault Model

Finite-fault excitation improves the P- and S-wave arrival times and amplitude ratios at multiple near-field sites not aligned with the main rupture direction, and it improves waveform fitting in the P-coda. These gains are consistent with directivity and finite-source effects that a point source cannot capture. At greater distances, improvements are modest for surface waves across frequency bands, showing that path structure dominates long-range dispersion and the coda. In practice, finite-fault inversions may prioritize near-field waveforms, whereas far-field fits are more dominated by the shallow velocity model.

Finite-fault models derived from InSAR inversion significantly improve the match to high-frequency waveforms at near-field stations, particularly at stations not aligned with the main rupture direction. This match demonstrates the advantage of finite-fault modeling in capturing rupture directivity (Figure 10). For small to moderate events ($M_w < 5$), it is often difficult to accurately estimate rupture parameters because of insufficient high-quality seismic data (McGuire, 2004). Many existing studies rely on empirical Green's functions derived from nearby small earthquakes to invert mainshock rupture processes, including rupture direction, fault length, and rupture velocity (Tan Y and Helmberger, 2010; Ye LL et al., 2022; Gong WZ et al., 2024; Luo Y et al., 2024). The proposed hybrid method can calculate a high-precision Green's function database for 3D velocity modeling and combine it with empirical Green's functions to jointly invert the rupture process. With improved finite-fault models inverted by both InSAR and seismic observations, we believe that the fit of high-frequency waveforms will be improved (McGuire, 2004; He X and Ni S, 2017, 2018).

4.5 Limitations and Future Work

Residuals of Rayleigh-wave time delays and azimuthal variations indicate that the shallow basin structure remains under-resolved. The Changning area features a complex shallow geological structure, and using a seismic reflection model may provide a better fit for the P-wave. Frequency-dependent attenuation is not explicitly modeled and could trade off with shallow velocity (Wei Z and Zhao L, 2019). Reliable surface-wave analysis depends on an accurate large-scale velocity model. In regions where the shallow structure is poorly constrained, high-frequency surface waves are strongly affected, particularly in terms of time delays. In contrast, P-waves are less sensitive to shallow structure in the large-scale velocity model (Monteiller et al., 2013; Wang Y et al., 2016). Thus, even when the large-scale velocity model is inaccurate, our proposed method can still be effectively applied to investigate the source-region velocity structure using the P-wave.

Because the one-time RSGT computation amortizes over many runs, data storage and I/O become important at higher frequencies and for larger station sets (e.g., Zhou L et al., 2016; Lo YC et al., 2018; Zang C et al., 2024). Future developments will leverage reciprocity-based injection strategies to further reduce cost, integrate improved shallow constraints from dense arrays and geological data, and couple InSAR-informed finite-fault models with high-frequency waveform inversions.

5. Conclusion

We developed a full 3D hybrid simulation method based on SEM, which stores precomputed boundary strain Green's functions for the small region studied. This method significantly improves forward-simulation efficiency when modifying only source parameters or near-source velocity models. Synthetic tests and real-data application in southern Sichuan demonstrate that the method is well-suited for accurate regional-scale wavefield modeling.

Combined simulations of source-region and large-scale velocity models reveal an apparent low-velocity sedimentary layer in the Changning region. Additionally, substantial arrival-time delays of high-frequency surface waves indicate that actual velocities above 5 km depth in the Sichuan Basin are lower than those presented in current models. Adding a low-velocity layer to the source region improves the fitting of high-frequency near-field waveforms. Because of the limited resolution of current models, further refinement will require high-resolution inversion methods and denser seismic observations. Finally, complex source models, such as a finite-fault model, better explain multi-band waveform features and rupture directivity observed in high-frequency data. Additional high-frequency datasets will be incorporated to perform source parameter inversion based on the validated 3D velocity model. In the future, waveform injection can also be utilized to efficiently compute the adjoint wavefield and sensitivity kernels within the source region, enabling a joint inversion of the source-region velocity structure and earthquake source parameters (Tape et al., 2007, 2009; Wang Y et al., 2016).

Acknowledgments

This study was supported by the National Key Research and Development Program of China (Grant No. 2020YFA0710600) and by the National Natural Science Foundation of China (Grant Nos. 42325401 and U1939202).

Data and Code Availability

The dataset used in this study is openly available on Zenodo at https://doi.org/10.5281/zenodo.17624366, and codes can be downloaded at https://github.com/planetarianPKU/HybridSGT-RT. The repository includes the codes for the hybrid 3D SEM simulation and a reproducible subset of the SGT database used to generate the examples in the manuscript. The full SGT dataset is readily available from the author upon request. All SGT datasets were generated using the SPECFEM3D_Cartesian package (Komatitsch and Tromp, 1999).

References

Aki, K., and Richards, P. G. (2002). *Quantitative Seismology* (2nd ed.). Herndon, Virginia: University Science Books.

Ba, Z. N., Han, S. J., Zhao, J. X., and Liu, Z. H. (2025). Effects of a 3D basin on the near-fault ground motion by an FK-FE hybrid method. *J. Appl. Geophys.*, *233*, 105581. https://doi.org/10.1016/j.jappgeo.2024.105581

Berg, E. M., Lin, F. C., Schulte-Pelkum, V., Allam, A., Qiu, H. R., and Gkogkas, K. (2021). Shallow crustal shear velocity and Vp/Vs across southern California: Joint inversion of short-period Rayleigh wave ellipticity, phase velocity, and teleseismic receiver functions. *Geophys. Res. Lett.*, *48*(15), e2021GL092626. https://doi.org/10.1029/2021GL092626

Brocher, T. M. (2005). Empirical relations between elastic wavespeeds and density in the Earth's crust. *Bull. Seismol. Soc. Am.*, *95*(6), 2081–2092.

https://doi.org/10.1785/0120050077

Chu, R. S., and Sheng, M. H. (2023). Stress features inferred from induced earthquakes in the Weiyuan shale gas block in southwestern China. *J. Geophys. Res.: Solid Earth*, *128*(2), e2022JB025344. https://doi.org/10.1029/2022JB025344

Clayton, R., and Engquist, B. (1977). Absorbing boundary conditions for acoustic and elastic wave equations. *Bull. Seismol. Soc. Am.*, *67*(6), 1529–1540. https://doi.org/10.1785/BSSA0670061529

Fichtner, A., and Tkalčić, H. (2010). Insights into the kinematics of a volcanic caldera drop: Probabilistic finite-source inversion of the 1996 Bárdarbunga, Iceland, earthquake. *Earth Planet. Sci. Lett.*, *297*(3-4), 607–615. https://doi.org/10.1016/j.epsl.2010.07.013

Gallovič, F., Käser, M., Burjánek, J., and Papaioannou, C. (2010). Three-dimensional modeling of near-fault ground motions with nonplanar rupture models and topography: Case of the 2004 Parkfield earthquake. *J. Geophys. Res.: Solid Earth*, *115*(B3), B03308. https://doi.org/10.1029/2008JB006171

Gong, W. Z., Ye, L. L., Xu, S. Q., Tan, Y. P., and Chen, X. F. (2024). Rupture behaviors of the southern Xianshuihe fault and seismicity around Mt. Gongga: Insights from the 2022 M_w 6.6 Luding (China) earthquake sequence. *Tectonophysics*, *892*, 230538. https://doi.org/10.1016/j.tecto.2024.230538

Graves, R., Jordan, T. H., Callaghan, S., Deelman, E., Field, E., Juve, G., Kesselman, C., Maechling, P., Mehta, G., … Vahi, K. (2011). CyberShake: A physics-based seismic hazard model for southern California. *Pure Appl. Geophys.*, *168*(3), 367–381. https://doi.org/10.1007/s00024-010-0161-6

Graves, R. W., and Wald, D. J. (2001). Resolution analysis of finite fault source inversion using one- and three-dimensional Green's functions: 1. Strong motions. *J. Geophys. Res.: Solid Earth*, *106*(B5), 8745–8766. https://doi.org/10.1029/2000JB900436

Guo, X. Q., Wang, Y., He, X. H., Luo, Y., and Zheng, K. Y. (2024). Research on the influence of velocity model uncertainty on source parameter waveform inversion based on numerical experiments. *Earthquake (in Chinese)*, *44*(4), 131–152. https://doi.org/10.12196/j.issn.1000-3274.2024.04.009

He, X., and Ni, S. (2017). Rapid rupture directivity determination of moderate dip-slip earthquakes with teleseismic body waves assuming reduced finite source approximation. *J. Geophys. Res.: Solid Earth*, *122*(7), 5344–5368. https://doi.org/10.1002/2016JB013924

He, X., and Ni, S. (2018). Resolving horizontal rupture directivity of moderate crustal earthquake in sparse network with ambient noise location. *J. Geophys. Res.: Solid Earth*, *123*(1), 533–552. https://doi.org/10.1002/2017JB014735

He, X. H., Zhang, P. Z., Ni, S. D., and Zheng, W. J. (2019). Resolving focal depth in sparse network with local depth phase *sPL*: A case study for the 2011 Mineral, Virginia, earthquake sequence. *Bull. Seismol. Soc. Am.*, *109*(2), 745–755. https://doi.org/10.1785/0120180221

Hejrani, B., Tkalčić, H., and Fichtner, A. (2017). Centroid moment tensor catalogue using a 3-D continental scale Earth model: Application to earthquakes in Papua New Guinea and the Solomon Islands. *J. Geophys. Res.: Solid Earth*, *122*(7), 5517–5543. https://doi.org/10.1002/2017JB014230

Hejrani, B., and Tkalčić, H. (2020). Resolvability of the centroid-moment-tensors for shallow seismic sources and improvements from modeling high-frequency waveforms. *J. Geophys. Res.: Solid Earth*, *125*(7), e2020JB019643. https://doi.org/10.1029/2020JB019643

Hsieh, M. C., Zhao, L., Ji, C., and Ma, K. F. (2016). Efficient inversions for earthquake slip distributions in 3D structures. *Seismol. Res. Lett.*, *87*(6), 1342–1354. https://doi.org/10.1785/0220160050

Hua, S. B., Xu, C. Y., Zhou, J. C., Xu, B. B., Feng, W. P., Zhang, Y., and Fang, L. H. (2024). Source characteristics and disaster mechanisms of the 2023 Gansu Jishishan M_w 6.0 earthquake. *Chinese J. Geophys. (in Chinese)*, *67*(7), 2625–2636. https://doi.org/10.6038/cjg2024S0089

Komatitsch, D., and Tromp, J. (1999). Introduction to the spectral element method for three-dimensional seismic wave propagation. *Geophys. J. Int.*, *139*(3), 806–822. https://doi.org/10.1046/j.1365-246x.1999.00967.x

Lay, T., Ye, L. L., Bai, Y. F., Cheung, K. F., and Kanamori, H. (2018). The 2018 M_w 7.9 Gulf of Alaska earthquake: Multiple fault rupture in the Pacific plate. *Geophys. Res. Lett.*, *45*(18), 9542–9551. https://doi.org/10.1029/2018GL079813

Lei, X. L., Huang, D. J., Su, J. R., Jiang, G. M., Wang, X. L., Wang, H., Guo, X., and Fu, H. (2017). Fault reactivation and earthquakes with magnitudes of up to Mw4.7 induced by shale-gas hydraulic fracturing in Sichuan Basin, China. *Sci. Rep.*, *7*(1), 7971. https://doi.org/10.1038/s41598-017-08557-y

Lei, X. L., Wang, Z. W., and Su, J. R. (2019a). The December 2018 M_L 5.7 and January 2019 M_L 5.3 earthquakes in South Sichuan basin induced by shale gas hydraulic fracturing. *Seismol. Res. Lett.*, *90*(3), 1099–1110. https://doi.org/10.1785/0220190029

Lei, X. L., Wang, Z. W., and Su, J. R. (2019b). Possible link between long-term and short-term water injections and earthquakes in salt mine and shale gas site in Changning, south Sichuan Basin, China. *Earth Planet. Phys.*, *3*(6), 510–525. https://doi.org/10.26464/epp2019052

Li, C., Yao, H. J., Yang, Y., Luo, S., Wang, K. D., Wan, K. S., Wen, J., and Liu, B. (2020). 3-D shear wave velocity structure in the shallow crust of the Tan-Lu fault zone in Lujiang, Anhui, and adjacent areas, and its tectonic implications. *Earth Planet. Phys.*, *4*(3), 317–328. https://doi.org/10.26464/epp2020026

Li, D. H., Zhan, Y., Ding, Z. F., Gao, J. Y., Wu, P. P., Meng, L. Y., Sun, X. Y., and Zhang, X. (2021). Upper crustal velocity and seismogenic environment of the Changning M_S 6.0 earthquake region in Sichuan, China. *Chinese J. Geophys. (in Chinese)*, *64*(1), 18–35. https://doi.org/10.6038/cjg2021O0241

Li, H. Y., Su, W., Wang, C. Y., and Huang, Z. X. (2009). Ambient noise Rayleigh wave tomography in western Sichuan and eastern Tibet. *Earth Planet. Sci. Lett.*, *282*(1-4), 201–211. https://doi.org/10.1016/j.epsl.2009.03.021

Liu, Q., and Gu, Y. J. (2012). Seismic imaging: From classical to adjoint tomography. *Tectonophysics, 566–567*, 31–66. https://doi.org/10.1016/j.tecto.2012.07.006

Liu, Q. X., Zhou, M., Tian, X. F., Qiu, Y., Shen, Z. C., Wang, Q. D., and Wang, C. P. (2023). High-resolution shear-wave velocity structure of the 2019 M_s 6.0 Changning earthquake region and its implication for induced seismicity. *Seismol. Res. Lett.*, *94*(3), 1392–1404. https://doi.org/10.1785/0220220253

Liu, T. S., Du, N. Q., Lei, T., Wang, K., He, B., Tong, P., Grasselli, G., and Liu, Q. Y. (2025). Seismic wavefield injection based on interface discontinuity: Theory and numerical implementation based upon the spectral-element method. *Geophys. J. Int.*, *241*(1), 658–673. https://doi.org/10.1093/gji/ggaf054

Liu, Y., Yu, Z. Y., Zhang, Z. Q., Yao, H. J., Wang, W. T., Zhang, H. J., Fang, H. J., and Fang, L. H. (2023). The high-resolution community velocity model V2.0 of southwest China, constructed by joint body and surface wave tomography of data recorded at temporary dense arrays. *Sci. China Earth Sci.*, *66*(10), 2368–2385. https://doi.org/10.1007/s11430-022-1161-7

Liu, Y. S., Xu, T., Wang, Y. H., Teng, J. W., Badal, J., and Lan, H. Q. (2019). An efficient source wavefield reconstruction scheme using single boundary layer values for the spectral element method. *Earth Planet. Phys.*, *3*(4), 342–357. https://doi.org/10.26464/epp2019035

Lo, Y. C., Zhao, L., Xu, X. W., Chen, J., and Hung, S. H. (2018). The 13 November 2016 Kaikoura, New Zealand earthquake: Rupture process and seismotectonic implications. *Earth Planet. Phys.*, *2*(2), 139–149. https://doi.org/10.26464/epp2018014

Long, F., Zhang, Z. W., Qi, Y. P., Liang, M. J., Ruan, X., Wu, W. W., Jiang, G. M., and Zhou, L. Q. (2020). Three dimensional velocity structure and accurate earthquake location in Changning–Gongxian area of southeast Sichuan. *Earth Planet. Phys.*, *4*(2), 163–177. https://doi.org/10.26464/epp2020022

Luo, H., Wang, T., and Wei, S. J. (2022). Systematic comparison of InSAR and seismic source models for moderate-size earthquakes in western China: Implication to the seismogenic capacity of the shallow crust. *J. Geophys. Res.: Solid Earth*, *127*(10), e2022JB024794. https://doi.org/10.1029/2022JB024794

Luo, Y., Zhao, L., and Zhu, Y. J. (2024). The rupture directivity study of moderate earthquakes using empirical Green's function approach: A case study of Panzhihua earthquake. *Chinese J. Geophys. (in Chinese)*, *67*(1), 144–155. https://doi.org/10.6038/cjg2023Q0475

Lyu, C., Zhao, L., and Capdeville, Y. (2022). Novel hybrid numerical simulation of the wave equation by combining physical and numerical representation theorems and a review of hybrid methodologies. *J. Geophys. Res.: Solid Earth*, *127*(5), e2021JB022368. https://doi.org/10.1029/2021JB022368

Lyu, C., Romanowicz, B., Zhao, L., and Masson, Y. (2025). Efficient hybrid numerical modeling of the seismic wavefield in the presence of solid-fluid boundaries. *Nat. Commun.*, *16*(1), 1722. https://doi.org/10.1038/s41467-025-56530-5

Ma, S. T. (2010). Focal depth determination for moderate and small earthquakes by modeling regional depth phases *sPg*, *sPmP*, and *sPn*. *Bull. Seismol. Soc. Am.*, *100*(3), 1073–1088. https://doi.org/10.1785/0120090103

Masson, Y., Cupillard, P., Capdeville, Y., and Romanowicz, B. (2014). On the numerical implementation of time-reversal mirrors for tomographic imaging. *Geophys. J. Int.*, *196*(3), 1580–1599. https://doi.org/10.1093/gji/ggt459

McGuire, J. J. (2004). Estimating finite source properties of small earthquake ruptures. *Bull. Seismol. Soc. Am.*, *94*(2), 377–393. https://doi.org/10.1785/0120030091

Monteiller, V., Chevrot, S., Komatitsch, D., and Fuji, N. (2013). A hybrid method to compute short-period synthetic seismograms of teleseismic body waves in a 3-D regional model. *Geophys. J. Int.*, *192*(1), 230–247. https://doi.org/10.1093/gji/ggs006

Neves, M., Chuang, L. Y., Li, W., Peng, Z. G., Figueiredo, P. M., and Ni, S. D. (2024). Complex rupture dynamics of the extremely shallow August 2020 M5.1 Sparta, North Carolina earthquake. *Commun. Earth Environ.*, *5*(1), 163. https://doi.org/10.1038/s43247-024-01316-8

Ni, H. Y., Li, J. L., Deng, B., Zhang, J. Y., Lu, Y. C., Zhao, Y., Chen, J. Y., and Su, P. (2025a). High-resolution shallow structures of the Red River fault zone in the southeastern Tibetan Plateau of China revealed by multiple seismic dense linear arrays. *Earth Planet. Phys.*, *9*(2), 195–211. https://doi.org/10.26464/epp2024076

Ni, H. Y., Li, J. L., Yao, H. J., Huang, X. L., Li, L. L., Zhou, D. R., Wang, X. L., Yu, S. Y., Lu, Y. C., … Li, H. P. (2025b). Preliminary study of the tectonic structure and seismogenic environment of the *M*4.7 Feidong earthquake sequence on September 18, 2024 in Hefei. *Earthq. Sci.*, *38*(3), 234–252. https://doi.org/10.1016/j.eqs.2024.11.001

Noe, S., van Herwaarden, D. P., Thrastarson, S., Pienkowska, M., Masouminia, N., Ma, J. C., Bunge, H. P., Wehner, D., Rawlinson, N., … Fichtner, A. (2024). The collaborative seismic Earth model: Generation 2. *J. Geophys. Res.: Solid Earth*, *129*(12), e2024JB029656. https://doi.org/10.1029/2024JB029656

Qian, Y. Y., Chen, X. F., Luo, H., Wei, S. J., Wang, T., Zhang, Z. G., and Luo, X. Y. (2019a). An extremely shallow M_w 4.1 thrust earthquake in the eastern Sichuan Basin (China) likely triggered by unloading during infrastructure construction. *Geophys. Res. Lett.*, *46*(23), 13775–13784. https://doi.org/10.1029/2019GL085199

Qian, Y. Y., Wei, S. J., Wu, W. B., Zeng, H. Y., Coudurier-Curveur, A., and Ni, S. D. (2019b). Teleseismic waveform complexities caused by near trench structures and their impacts on earthquake source study: Application to the 2015 Illapel aftershocks (Central Chile). *J. Geophys. Res.: Solid Earth*, *124*(1), 870–889. https://doi.org/10.1029/2018JB016143

Qian, Y. Y., Chen, X. F., Wu, W. B., Wei, S. J., Ni, S. D., Xu, M., Qin, Y. F., Nakamura, Y., Zhou, Y., and Sun, D. Y. (2024). Patterns of causative faults of normal earthquakes in the fluid-rich outer rise of northeastern Japan, constrained with 3D teleseismic waveform modeling. *J. Geophys. Res.: Solid Earth*, *129*(6), e2024JB028740. https://doi.org/10.1029/2024JB028740

Shao, X. H., Yao, H. J., Liu, Y., Yang, H. F., Tian, B. F., and Fang, L. H. (2022). Shallow crustal velocity structures revealed by active source tomography and fault activities of the Mianning–Xichang segment of the Anninghe fault zone, Southwest China. *Earth Planet. Phys.*, *6*(2), 204–212. https://doi.org/10.26464/epp2022010

Sheng, M. H., Chu, R. S., Ni, S. D., Wang, Y., Jiang, L. M., and Yang, H. F. (2020). Source parameters of three moderate size earthquakes in Weiyuan, China, and their relations to shale gas hydraulic fracturing. *J. Geophys. Res.: Solid Earth*, *125*(10), e2020JB019932. https://doi.org/10.1029/2020JB019932

Sheng, M. H., Chu, R. S., Peng, Z. G., Wei, Z. G., Zeng, X. F., Wang, Q. D., and Wang, Y. (2022). Earthquakes triggered by fluid diffusion and boosted by fault reactivation in Weiyuan, China due to hydraulic fracturing. *J. Geophys. Res.: Solid Earth*, *127*(5), e2021JB022963. https://doi.org/10.1029/2021JB022963

Shi, Q. B., Wei, S. J., and Chen, M. (2018). An MCMC multiple point sources inversion scheme and its application to the 2016 Kumamoto M_w 6.2 earthquake. *Geophys. J. Int.*, *215*(2), 737–752. https://doi.org/10.1093/gji/ggy302

Stacey, R. (1988). Improved transparent boundary formulations for the elastic-wave equation. *Bull. Seismol. Soc. Am.*, *78*(6), 2089–2097. https://doi.org/10.1785/BSSA0780062089

Tan, Y., and Helmberger, D. (2010). Rupture directivity characteristics of the 2003 Big Bear sequence. *Bull. Seismol. Soc. Am.*, *100*(3), 1089–1106. https://doi.org/10.1785/0120090074

Tan, Y. Y., Hu, J., Zhang, H. J., Chen, Y. K., Qian, J. W., Wang, Q. F., Zha, H., Tang, P., and Nie, Z. (2020). Hydraulic fracturing induced seismicity in the southern Sichuan Basin due to fluid diffusion inferred from seismic and injection data analysis. *Geophys. Res. Lett.*, *47*(4), e2019GL084885. https://doi.org/10.1029/2019GL084885

Tan, Y. Y., Qian, J. W., Hu, J., Zhang, H. J., Xing, H. L., Li, J. L., Xu, J., Yang, W., Gu, N., and Miao, S. Y. (2023). Tomographic evidences for hydraulic fracturing induced seismicity in the Changning shale gas field, southern Sichuan Basin, China. *Earth Planet. Sci. Lett.*, *605*, 118021. https://doi.org/10.1016/j.epsl.2023.118021

Tang, C. X., Chen, L., and Wang, X. (2022). Shear-wave velocity structures of the shallow crust beneath the Ordos and Sichuan Basins from multi-frequency direct P-wave amplitudes in receiver functions. *Sci. China Earth Sci.*, *65*(5), 810–823. https://doi.org/10.1007/s11430-021-9884-2

Tape, C., Liu, Q. Y., and Tromp, J. (2007). Finite-frequency tomography using adjoint methods—Methodology and examples using membrane surface waves. *Geophys. J. Int.*, *168*(3), 1105–1129. https://doi.org/10.1111/j.1365-246X.2006.03191.x

Tape, C., Liu, Q. Y., Maggi, A., and Tromp, J. (2009). Adjoint tomography of the southern California crust. *Science*, *325*(5943), 988–992. https://doi.org/10.1126/science.1175298

Tian, W., Wu, Q. J., Dai, K., Guo, R. M., Yao, Z. X., Qiang, Z. Y., and Deng, F. (2024). Seismological evidence for the existence of long-distance hydrological channel and its implication for fluid overpressure in southern Sichuan, China. *Geophys. Res. Lett.*, *51*(8), e2023GL107167. https://doi.org/10.1029/2023GL107167

Wang, M. M., Hubbard, J., Plesch, A., Shaw, J. H., and Wang, L. N. (2016). Three-dimensional seismic velocity structure in the Sichuan basin, China. *J. Geophys. Res.: Solid Earth*, *121*(2), 1007–1022. https://doi.org/10.1002/2015JB012644

Wang, N., Shen, Y., Bao, X. Y., and Flinders, A. (2019). Locating shallow seismic sources with waves scattered by surface topography: Validation of the method at the Nevada Test Site. *J. Geophys. Res.: Solid Earth*, *124*(7), 7040–7051. https://doi.org/10.1029/2018JB017291

Wang, Q., Li, S. Y., Li, X. Y., Wu, Y., Zhao, P. P., and Gao, Y. (2024). Deep tectonics and seismogenic mechanisms of the seismic source zone of the Jishishan M_S 6.2 earthquake on December 18, 2023, at the northeast margin of the Tibetan Plateau. *Earth Planet. Phys.*, *8*(3), 514–521. https://doi.org/10.26464/epp2024024

Wang, S., Jiang, G. Y., Lei, X. L., Barbour, A. J., Tan, X. B., Xu, C. J., and Xu, X. W. (2022). Three Mw ≥ 4.7 earthquakes within the Changning (China) shale gas field ruptured shallow faults intersecting with hydraulic fracturing wells. *J. Geophys. Res.: Solid Earth*, *127*(2), e2021JB022946. https://doi.org/10.1029/2021JB022946

Wang, X., and Zhan, Z. W. (2020). Seismotectonics and fault geometries of the 2019 Ridgecrest sequence: Insight from aftershock moment tensor catalog using 3-D Green's functions. *J. Geophys. Res.: Solid Earth*, *125*(5), e2020JB019577. https://doi.org/10.1029/2020JB019577

Wang, X., Chen, L., and Chen, Q. F. (2024). Evaluation of 3D crustal seismic velocity models in southwest China: Model performance, limitation, and prospects. *Sci. China Earth Sci.*, *67*(2), 604–619. https://doi.org/10.1007/s11430-023-1215-1

Wang, Y., Chevrot, S., Monteiller, V., Komatitsch, D., Mouthereau, F., Manatschal, G., Sylvander, M., Diaz, J., Ruiz, M., … Martin, R. (2016). The deep roots of the western Pyrenees revealed by full waveform inversion of teleseismic P waves. *Geology*, *44*(6), 475–478. https://doi.org/10.1130/G37812.1

Wei, S. J., Helmberger, D., Owen, S., Graves, R. W., Hudnut, K. W., and Fielding, E. J. (2013). Complementary slip distributions of the largest earthquakes in the 2012 Brawley swarm, Imperial Valley, California. *Geophys. Res. Lett.*, *40*(5), 847–852. https://doi.org/10.1002/grl.50259

Wei, S. J., Avouac, J. P., Hudnut, K. W., Donnellan, A., Parker, J. W., Graves, R. W., Helmberger, D., Fielding, E., Liu, Z., … Eneva, M. (2015). The 2012 Brawley swarm triggered by injection-induced aseismic slip. *Earth Planet. Sci. Lett.*, *422*, 115–125. https://doi.org/10.1016/j.epsl.2015.03.054

Wei, Z., and Zhao, L. (2019). Lg-Q model and its implication on high-frequency ground motion for earthquakes in the Sichuan and Yunnan region. *Earth Planet. Phys.*, *3*(6), 526–536. https://doi.org/10.26464/epp2019054

Wei, Z. G., Chu, R. S., Chen, L., Wu, S. S., Jiang, H., and He, B. (2020). The structure of the sedimentary cover and crystalline crust in the Sichuan Basin and its tectonic implications. *Geophys. J. Int.*, *223*(3), 1879–1887. https://doi.org/10.1093/gji/ggaa420

Wu, J. P., Cai, Y., Wang, W., Wang, W. L., Wang, C. Z., Fang, L. H., Liu, Y. N., and Liu, J. (2024). Three-dimensional velocity model and its tectonic implications at China Seismic Experimental Site, eastern margin of the Tibetan Plateau. *Sci. China Earth Sci.*, *67*(7), 2268–2290. https://doi.org/10.1007/s11430-023-1293-4

Wu, W. B., Ni, S. D., Zhan, Z. W., and Wei, S. J. (2018). An SEM-DSM three-dimensional hybrid method for modelling teleseismic waves with complicated source-side structures. *Geophys. J. Int.*, *215*(1), 133–154. https://doi.org/10.1093/gji/ggy273

Xiao, X., Cheng, S. H., Wu, J. P., Wang, W. L., Sun, L., Wang, X. X., and Wen, L. X. (2021). Shallow seismic structure beneath the continental China revealed by *P*-wave polarization, Rayleigh wave ellipticity and receiver function. *Geophys. J. Int.*, *225*(2), 998–1019. https://doi.org/10.1093/gji/ggab022

Xiao, X., Cheng, S. H., Wu, J. P., Wang, W. L., Sun, L., Wang, X. X., Ma, J. Y., Tong, Y. H., Liang, X. F., … Wen, L. X. (2024). CSRM-1.0: A China seismological reference model. *J. Geophys. Res.: Solid Earth*, *129*(9), e2024JB029520. https://doi.org/10.1029/2024JB029520

Xie, Z. N., Komatitsch, D., Martin, R., and Matzen, R. (2014). Improved forward wave propagation and adjoint-based sensitivity kernel calculations using a numerically stable finite-element PML. *Geophys. J. Int.*, *198*(3), 1714–1747. https://doi.org/10.1093/gji/ggu219

Xie, Z. N., Matzen, R., Cristini, P., Komatitsch, D., and Martin, R. (2016). A perfectly matched layer for fluid-solid problems: Application to ocean-acoustics simulations with solid ocean bottoms. *J. Acoust. Soc. Am.*, *140*(1), 165–175. https://doi.org/10.1121/1.4954736

Xu, T. R., Yang, Z. G., Dai, D. Q., Zhi, M., Zhang, J. Y., Du, G. B., Xi, N., and Sun, L. (2025). The seismic mechanisms and seismogenic environment of the M_S 6.2 earthquake in Jishishan, Gansu, China: Evidence from relocation, focal mechanisms, and rupture processes. *Earth Planet. Phys.*, *9*(2), 309–322. https://doi.org/10.26464/epp2025016

Yang, H. F. (2015). Recent advances in imaging crustal fault zones: A review. *Earthq. Sci.*, *28*(2), 151–162. https://doi.org/10.1007/s11589-015-0114-3

Yang, W., Chen, G. Y., Meng, L. Y., Zang, Y., Zhang, H. J., and Li, J. L. (2021). Determination of the local magnitudes of small earthquakes using a dense seismic array in the Changning–Zhaotong Shale Gas Field, Southern Sichuan Basin. *Earth Planet. Phys.*, *5*(6), 532–546. https://doi.org/10.26464/epp2021026

Yang, Z. G., Liu, J., Zhang, Y. Y., Yang, W., and Zhang, X. M. (2024). Rapid report of source parameters of 2023 *M*6.2 Jishishan, Gansu earthquake sequence. *Earth Planet. Phys.*, *8*(2), 436–443. https://doi.org/10.26464/epp2024012

Yao, H. J. (2020). Building the community velocity model in the Sichuan-Yunnan region, China: Strategies and progresses. *Sci. China Earth Sci.*, *63*(9), 1425–1428. https://doi.org/10.1007/s11430-020-9645-3

Ye, L. L., Bai, Y. F., Si, D. J., Lay, T., Cheung, K. F., and Kanamori, H. (2022). Rupture model for the 29 July 2021 M_W 8.2 Chignik, Alaska earthquake constrained by seismic, geodetic, and tsunami observations. *J. Geophys. Res.: Solid Earth*, *127*(7), e2021JB023676. https://doi.org/10.1029/2021JB023676

Yi, G. X., Long, F., Liang, M. J., Zhao, M., Wang, S. W., Gong, Y., Qiao, H. Z., and Su, J. R. (2019). Focal mechanism solutions and seismogenic structure of the 17 June 2019 M_S 6.0 Sichuan Changning earthquake sequence. *Chinese J. Geophys. (in Chinese)*, *62*(9), 3432–3447. https://doi.org/10.6038/cjg2019N0297

Yi, G. X., Long, F., Liang, M. J., Zhao, M., Zhang, H. P., Zhou, R. J., Li, Y., Liu, H., Wu, P., … Su, J. R. (2023). Seismogenic structure of the 5 September 2022 Sichuan Luding M_S 6.8 earthquake sequence. *Chinese J. Geophys. (in Chinese)*, *66*(4), 1363–1384. https://doi.org/10.6038/cjg2023Q0923

Zang, C., Wu, W. B., Ni, S. D., and Xu, M. (2024). A reciprocity-based efficient method for improved source parameter estimation of submarine earthquakes with hybrid 3-D teleseismic Green's functions. *J. Geophys. Res.: Solid Earth*, *129*(5), e2023JB028174. https://doi.org/10.1029/2023JB028174

Zeng, Q., Chu, R. S., Sheng, M. H., and Wei, Z. G. (2020). Seismic ambient noise tomography for shallow velocity structures beneath Weiyuan, Sichuan. *Chinese J. Geophys. (in Chinese)*, *63*(3), 944–955. https://doi.org/10.6038/cjg2020N0177

Zhang, L., Hao, J. L., Deng, W. Z., Ji, C., and Zhang, C. H. (2022). Source parameters inversion of the global large earthquakes using 3-D SEM Green's functions: Strain Green's function calculation and validation. *Geophys. J. Int.*, *230*(3), 1546–1564. https://doi.org/10.1093/gji/ggac135

Zhao, L., Jordan, T. H., and Chapman, C. H. (2000). Three-dimensional Fréchet differential kernels for seismic delay times. *Geophys. J. Int.*, *141*(3), 558–576. https://doi.org/10.1046/j.1365-246x.2000.00085.x

Zhao, L., Chen, P., and Jordan, T. H. (2006). Strain Green's tensors, reciprocity, and their applications to seismic source and structure studies. *Bull. Seismol. Soc. Am.*, *96*(5), 1753–1763. https://doi.org/10.1785/0120050253

Zhao, L. S., and Helmberger, D. V. (1994). Source estimation from broadband regional seismograms. *Bull. Seismol. Soc. Am.*, *84*(1), 91–104. https://doi.org/10.1785/BSSA0840010091

Zhou, L., Zhang, W., Shen, Y., Chen, X. F., and Zhang, J. (2016). Location and moment tensor inversion of small earthquakes using 3D Green's functions in models with rugged topography: Application to the Longmenshan fault zone. *Earthq. Sci.*, *29*(3), 139–151. https://doi.org/10.1007/s11589-016-0156-1

Zhou, P. C., Ellsworth, W. L., Yang, H. F., Tan, Y. J., Beroza, G. C., Sheng, M. H., and Chu, R. S. (2021). Machine-learning-facilitated earthquake and anthropogenic source detections near the Weiyuan Shale Gas Blocks, Sichuan, China. *Earth Planet. Phys.*, *5*(6), 501–519. https://doi.org/10.26464/epp2021053

Zhu, G. H., Yang, H. F., Tan, Y. J., Jin, M. P., Li, X. B., and Yang, W. (2022). The cascading foreshock sequence of the M_S 6.4 Yangbi earthquake in Yunnan, China. *Earth Planet. Sci. Lett.*, *591*, 117594. https://doi.org/10.1016/j.epsl.2022.117594

Zhu, L. P., and Helmberger, D. V. (1996). Advancement in source estimation techniques using broadband regional seismograms. *Bull. Seismol. Soc. Am.*, *86*(5), 1634–1641. https://doi.org/10.1785/BSSA0860051634

Zhu, L. P., and Ben-Zion, Y. (2013). Parametrization of general seismic potency and moment tensors for source inversion of seismic waveform data. *Geophys. J. Int.*, *194*(2), 839–843. https://doi.org/10.1093/gji/ggt137

Zuo, K. Z., Zhao, C. P., and Zhang, H. J. (2020). 3D crustal structure and seismicity characteristics of Changning–Xingwen area in the southwestern Sichuan basin, China. *Bull. Seismol. Soc. Am.*, *110*(5), 2154–2167. https://doi.org/10.1785/0120200085